This is to certify that the
thesis entitled

Statistical Correlations in Relativistic Heavy Ion Collisions

presented by

Silvio Petriconi

has been accepted towards fulfillment
of the requirements for the

M.S. degree in Physics

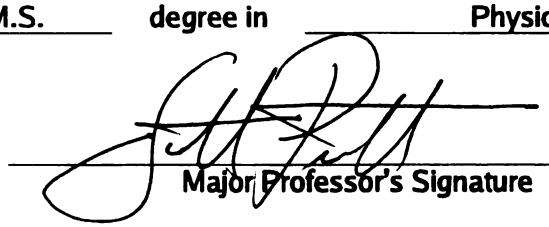

Major Professor's Signature

08/20/03

Date

STATISTICAL CORRELATIONS IN RELATIVISTIC HEAVY ION COLLISIONS

By

Silvio Petriconi

A THESIS

Submitted to
Michigan State University
in partial fulfillment of the requirements
for the degree of

MASTER OF SCIENCE

Department of Physics and Astronomy

2003

Thesis Adviser: Dr. Scott Pratt

ABSTRACT

STATISTICAL CORRELATIONS IN RELATIVISTIC HEAVY ION COLLISIONS

By

Silvio Petriconi

In order to understand the state of matter produced in relativistic heavy ion collisions, it is crucial to understand the space-time characteristics of the emitting source. Whereas the momenta of particles can be directly measured, space-time information can only be inferred from two-particle correlation observables. In this thesis, two different kind of correlation observables will be discussed:

Part I will investigate the two-particle correlation function for non-identical particles. It will be shown that the correlator is affected by Coulomb and strong final-state interactions in a way which allows extracting the size and lifetime of the source.

Part II will discuss the modeling of particle multiplicities for charge balance functions. The thermal model of a canonical ensemble under charge conservation constraints will be used to generate particle multiplicities at various temperatures. A highly optimized algorithm will be developed for calculating the partition functions iteratively. Balance functions obtained using this thermal model and the blast-wave description will be compared to experimental data, and good agreement will be seen.

To my parents

ACKNOWLEDGMENTS

This thesis would not have been possible without the strong support of many people and organizations. I am deeply indebted to my adviser, Dr. Scott Pratt, for his strong academic support, his patience and his financial assistance. I wish to thank Dr. Wolfgang Bauer for giving me the opportunity of spending an enriching and interesting year of studies at MSU. I gratefully acknowledge the support of the Studienstiftung des deutschen Volkes which gave me orientation and motivation during the entire period of my studies.

There have been many people who have been giving me understanding and moral support whenever I needed it. Special thanks are due to my family, and to my friends Andreas Glaser and Kristina Wagner for giving me encouragement and motivation in some critical moments.

Table of Contents

List of Tables

List of Figures

Chapter 1

Introduction

When speaking of the nucleus of an atom, we are used to thinking of it as a quantum mechanical composite object consisting of finite-size particles, protons and neutrons. However, one should realize that this picture is only a good description of a special phenomenology that we observe at lower energies. Neutrons and protons are not true elementary particles as we know from early high-energy physics experiments. Instead, they show the behaviour of a composite system consisting of three quarks which interact strongly with each other by the exchange of gluons. Unlike any other composite system in physics, the constituents of protons, neutrons or any other bound quark system cannot be observed individually as any attempt of separation is immediately followed by the creation of a new composite system.

This quark confinement phenomenon comes from the special long-range nature of the strong force and its explanation requires non-perturbative models. Lattice QCD provides a numerical treatment from first principles by evaluating the partition function through

randomly sampling the many-body quantum state. By performing these calculations at finite temperature, lattice QCD can give the equation of state and phase structure of the QCD vacuum. These calculations suggest that a deconfined state of quarks and gluons may exist at temperatures above $150 - 200$ MeV, or at energy densities of $1 - 3$ GeV/fm^3, respectively [33, 34]. At these temperatures, a nucleus would undergo a phase transition and form a quark-gluon-plasma (QGP) in which the major degrees of freedom are quarks and gluons rather than neutrons and protons. However, as this result is a purely theoretical prediction, it is now of significant interest to obtain experimental confirmation.

The latest generation of relativistic heavy ion colliders was designed to operate clearly above the critical energy density for the formation of a QGP in order to search for experimental evidence for this phenomenon. However, since such a quark-gluon plasma intermediate state is short-lived and quarks are reconfined after a time as short as a few fm/c, the most challenging part of the search for the quark-gluon plasma in heavy ion collisions is to find observables that can give a clear indication whether or not an intermediate QGP state was formed during the collision.

Many such observables ("QGP signals") have been suggested over the last two decades [15]:

- J/ψ suppression due to QGP screening of the $c - \bar{c}$ potential [42, 17]
- Strangeness enhancement [36, 53]
- Charge correlations [13, 4]
- Dileptons [2, 59, 8, 55]

- Flow [22, 21, 57]
- Jet quenching [27, 25, 11, 10, 12, 3, 5, 7]
- HBT measurements of lifetime [44, 56, 54]

In the first chapters of this thesis, we will investigate the last topic concerning statistical correlations in momentum space of the particles that are emitted in the collision process. Whilst identical boson correlations have been used exhaustively in Hanbury-Brown Twiss (HBT) interferometry to measure the size and lifetime of sources from which these particles were emitted [48, 61], relatively little attention has been paid to correlations of non-identical particles [41, 58, 39]. These correlations are caused by final-state Coulomb and strong interactions rather than through identical-particle interference. It will be shown that such correlations can give important information on source parameters especially those that are associated with the lifetime of the source. These are especially relevant since a phase transition, and the associated latent heat, should lead to a reduced pressure and an extended lifetime for emission.

The second part of this thesis will discuss charge balance functions as suggested in [13]. These functions exploit the constraint of local charge conservation in a heavy ion collision and are a promising candidate for a QGP signal. From analysis of relative rapidities of particles and their balancing partners, one can infer the timing of hadronization. In this thesis, we will develop an implementation of a thermal model for generating particle multiplicities under charge conservation constraints. The predictions of the thermal model will finally be compared against the shape of the balance function that has been measured at STAR [4].

Part I

Final-state Correlations of non-identical Particles

Chapter 2

Formalism of Correlation Functions

2.1 Introduction

Statistical correlations in momentum space of particle pairs were initially used in astronomy by Hanbury-Brown and Twiss to measure the size of distant stellar objects [28]. Later, Hanbury-Brown Twiss (HBT) interferometry also became a standard method in heavy ion physics [44, 29, 61] for investigating the size and lifetime of the emitting source, i.e. the distribution of space-time coordinates for which the final-state measured particles experienced their last interaction. The basic idea of HBT measurements is that particles emitted by a chaotic source are initially statistically uncorrelated. On their way from the source to the detector, however, identical bosons are affected by quantum mechanical Bose-Einstein symmetrization. This results in an enhancement in the coincidence probability for two particles with similar momenta. By fitting the measured coincidence probabilities of identical bosons to model-generated data, source sizes can be estimated.

In relativistic heavy ion physics, source sizes provide important information on the physics of the intermediate state. If a quark-gluon plasma is formed and the phase transition involves a significant amount of latent heat, it is expected that the lifetime of the emitting source would increase significantly [44, 54].

If the emission probability for a particle with velocity $\mathbf{v}$ at spacetime point $(t, \mathbf{x})$ is $S(t, \mathbf{x}, \mathbf{v})$, the correlation function is determined through the object

$$g(\mathbf{r}, \mathbf{v}) \equiv \frac{\int d^4x_1 d^4x_2 S_1(x_1, \mathbf{v}) S_2(x_2, \mathbf{v}) \delta^3(\mathbf{r} - (\mathbf{x}_1 - \mathbf{x}_2 - \mathbf{v}(t_1 - t_2)))}{\int d^4x_1 \int d^4x_2 S_1(x_1, v) S_2(x_2, v)} \tag{2.1}$$

which defines the probability that particles of type A and B with the same velocity $\mathbf{v}$ would be separated by $\mathbf{r}$ after emission. A long-lived source would lead to a shape of g which is significantly longer in the direction of $\mathbf{v}$, also called the "outwards" direction. For relativistic heavy ion physics it is the convention to define $\mathbf{v}$ in a frame moving along the beam axis such that the component of $\mathbf{p} = \mathbf{p}_a + \mathbf{p}_b$ along the beam is zero. Thus, $\mathbf{v}$ is manifestly perpendicular to the beam axis. The shape of g in the other two directions – the "longitudinal" direction along the beam axis and the "sidewards" direction that is perpendicular to the two others would not be affected by the lifetime. Correlation analyses measure the characteristic radii of g in these three directions. Assuming that $S(x, t)$ has comparable outward and sideward sizes in the lab frame, its lifetime can then be estimated by

$$v^2\tau^2 \approx R_{\text{out}}^2(1 - v^2/c^2) - R_{\text{side}}^2 \tag{2.2}$$

where R_{out} and R_{side} are the experimentally inferred dimensions of g in the two-particle

rest frame.

Remarkably, HBT correlation analyses at RHIC have shown nearly equal outward and sideward source sizes [6] which indicates extremely sudden emission. This strongly contradicts theoretical models involving a first-order phase transition. As this result comes quite unexpected, alternative methods for confirming these findings were explored. One of these methods is the use of non-identical particle correlations that will be discussed here.

It was noticed early in HBT interferometry that aside from Bose-Einstein symmetrization, significant additional correlations arise due to Coulomb and strong final-state interactions between the particle pair. These additional correlations have been investigated exhaustively [9, 60, 14] with the aim of correcting for them. Non-identical particles do not have any (anti-)symmetrization of their final states. Their correlations are dominated by Coulomb and strong FSI effects which for a long time were considered to be of little value in measuring the shape of $g(\mathbf{r})$. In the following chapters, it will be shown that strong and Coulomb induced correlations provide equivalent information for the lifetime and spatial extent of the source and can be used to independently verify HBT results.

2.2 The general FSI correlator

The two-particle correlation function is a measure for the enhancement in probability $P_2(\mathbf{p}_a, \mathbf{p}_b)$ to detect two particles from the same event at momenta $\mathbf{p}_a$ and $\mathbf{p}_b$, so if $P_1(\mathbf{p}_a)$ and $P_1(\mathbf{p}_b)$ are used to designate the corresponding one-particle probabilities, one defines the correlation function as

$$C(\mathbf{p}_a, \mathbf{p}_b) \equiv \frac{P_2(\mathbf{p}_a, \mathbf{p}_b)}{P_1(\mathbf{p}_a) P_1(\mathbf{p}_b)} \tag{2.3}$$

For non-identical particles, we will now show that this enhancement is approximately given by folding the square of the nonrelativistic wavefunction that solves the Schrödinger equation for the relative motion with the source emission function $g(\mathbf{r})$,

$$C(\mathbf{q}, \mathbf{v}) = \int d^3 r_0 \; g(\mathbf{r}_0, \mathbf{v}) \, |\psi(\mathbf{r}_0, \mathbf{q})|^2 \tag{2.4}$$

Here, $\mathbf{q}$ is the relative momentum of the two-particles in their center-of-mass frame. For particles without interaction, the wavefunction would be a plane wave and the correlator would be unity since $g(\mathbf{r})$ is normalized to unity. Interactions between the particles distort the wavefunction and give higher weight to certain regions of relative momentum which results in the observable structure of the correlator.

The derivation starts with considering the quantum-mechanical two-particle $\mathcal{T}$-matrix element $\mathcal{T}(x_1, x_2)$: If one could draw a complete Feynman diagram in coordinate space of the entire collision process, one could factorize it into an horribly complicated part $\mathcal{T}$ where all particles interact in arbitrary ways, and into another well-understood part U in which only the two particles that are finally detected at $t \to \infty$ with momenta $\mathbf{p}_a$ and $\mathbf{p}_b$ continue interacting with each other. We will label the two vertices where the diagram is factorized x_1 and x_2.

The total two-particle probability is the sum of the squared amplitudes of all diagrams which have a such a factorisable two-particle part with an asymptotic outgoing state

$|\mathbf{p}_a, \mathbf{p}_b\rangle$, so

$$P_2(\mathbf{p}_a, \mathbf{p}_b) = \sum_f \left| \int d^4x_1 d^4x_2 \mathcal{T}_f(x_1, x_2) U(x_1, x_2, p_a, p_b) \right|^2 \tag{2.5}$$

Just as in HBT interferometry [45], one can assume fully chaotic emission behaviour of the source. This is equivalent to requiring that the two-particle $\mathcal{T}$-matrix should simply be the product of two one-particle $\mathcal{T}$-matrices:

$$\mathcal{T}_f(x_1, x_2) \approx \mathcal{T}_{fa}(x_1)\mathcal{T}_{fb}(x_2) \tag{2.6}$$

It is technically convenient to change from the complex-valued amplitude $\mathcal{T}$ into a Wigner density $S(x, K)$ defined by

$$S(x, K) \equiv \sum_a \frac{1}{(2\pi)^4} \int d^4y \; e^{iK\cdot y} \mathcal{T}_a^*(x + \frac{y}{2}) \mathcal{T}_a(x - \frac{y}{2}) \tag{2.7}$$

Wigner densities are real but not necessarily positive definite. They contain all phase-space emission characteristics of the source and can be used like a probability density for particle emission at point x with momentum K as long as one of these two parameters is integrated over. The probability for one-particle emission with momentum $\mathbf{p}$ therefore is

$$P_1(\mathbf{p}) = \int d^4x \; S(x, p)\Big|_{p^0 = E_K} \tag{2.8}$$

The two-particle emission probability can also be expressed in terms of the Wigner density

S. One can separate the asymptotic center-of-mass motion of the two particles

$$U(x_1, x_2, p_a, p_b) \equiv \exp\left(iK \cdot \frac{m_a x_1 + m_b x_2}{m_a + m_b}\right) u(x_1 - x_2, k) \tag{2.9}$$

where $K = p_a + p_b$ and $k = (m_b p_a - m_a p_b)/(m_a + m_b)$ are the total and the relative four-momenta of the two particles. Note that this separation is essentially non-relativistic. For relativistic particle pairs it still holds as long as the relative particle momenta after a boost to the center-of-mass frame are non-relativistic. The particle pairs investigated in correlation analyses have usually sufficiently low momenta to satisfy this requirement.

The next step is to define the Wigner transformed W_k of the relative FSI interaction matrix element

$$W_k(q, x) \equiv \frac{1}{(2\pi)^4} \int d^4y \; e^{iq\cdot y} u^*(x + y/2, k) u(x - y/2, k) \tag{2.10}$$

By performing Fourier transforms of S, one can re-express the $\mathcal{T}$- and U-matrix elements in terms of the corresponding Wigner functions. Equation (2.5) then reads

$$\begin{aligned} P(\mathbf{p}_a, \mathbf{p}_b) &= \int d^4q \, d^4x_1 d^4x_2 \; S\left(x_1, \frac{m_a K}{m_a + m_b} + q\right) \\ &\times \; S\left(x_2, \frac{m_b K}{m_a + m_b} - q\right) W_k(q, x_2 - x_1) \end{aligned} \tag{2.11}$$

The densities S have a clear physical interpretation as emission (pseudo-)probability densities of the source. If the product of S_1 and S_2 is largely independent of q, one can make the so-called smoothness approximation and neglect the entire q dependence in $S_1 S_2$. For

systems with a broad $\mathcal{T}$ matrix element this assumption is safe, and for instantaneous thermal models it is even exact since the product of the two functions gives $\propto \exp(E_1 + E_2)$ which is independent of q. If the q dependence can be entirely neglected, the dq integration gives a delta function in y, and one obtains

$$P(\mathbf{p}_a, \mathbf{p}_b) = \int d^4x_1\, d^4x_2 S\left(x_1, \frac{m_a K}{m_a + m_b}\right) S\left(x_2, \frac{m_b K}{m_a + m_b}\right) u^*(x_2 - x_1, k) u(x_2 - x_1, k) \tag{2.12}$$

If the emission of the two particles would be simultaneous, further simplification would be possible since the u^*u matrix element would then become the wavefunction of the corresponding field. After boosting into the $K = 0$ frame, $x' = \Lambda(K)x$, one can make the ansatz that the particle that was emitted earlier will propagate along the classical trajectory of free motion with velocity $\mathbf{v}$ until the second particle is emitted. The matrix element u^*u is then taken at equal time $t' = t'_2$. This gives the wavefunction $|\psi(\mathbf{k}', \mathbf{x}'_2 - \mathbf{x}'_1 - \mathbf{v}(t'_2 - t'_1))|^2$ of the underlying field. Even though the fields of pions, protons, kaons and Ξ particles are relativistic spin 0 and spin 1/2 fields, the relative motion in the center-of-mass frame can be qualitatively described by a Schrödinger field as long as the relative momenta in the $K = 0$ frame are in the non-relativistic regime. The corresponding wavefunction will then be a solution of the Schödinger equation that describes the relative motion of the particle pair. As the Schrödinger equation is well-investigated for a large class of problems, the charm of this method is that all the wealth of information on how to treat such interactions in nonrelativistic quantum mechanics becomes available for use in final-state correlation analyses.

The two-particle probability in the c.o.m. frame finally reads

$$P_2(\mathbf{v},\mathbf{q}) = \int d^4x_1' \int d^4x_2' \int d^3r_0 S(x_1',\mathbf{v}) S(x_2',\mathbf{v}) \delta^3(\mathbf{r}_0 - \mathbf{x}_1' - \mathbf{x}_2' - \mathbf{v}(t_1' - t_2'))) \, |\psi(\mathbf{r}_0,\mathbf{q})|^2 \tag{2.13}$$

Here, $\mathbf{q}$ is the relative momentum in the c.o.m. frame.

Performing the d^4x_1 and d^4x_2 integration and dividing by the corresponding one-particle probabilities (2.8) one obtains for the final-state correlator the result

$$C(\mathbf{v},\mathbf{q}) = \int d^3r_0 \, g(\mathbf{v},\mathbf{r}_0) \, |\psi(\mathbf{r}_0,\mathbf{q})|^2 \tag{2.14}$$

$$g(\mathbf{v},\mathbf{r}_0) \equiv \frac{\int d^4x_1' \int d^4x_2' S(x_1',\mathbf{v}) S(x_2',\mathbf{v}) \delta^3(\mathbf{r}_0 - \mathbf{x}_1' - \mathbf{x}_2' - \mathbf{v}(t_1' - t_2'))}{\int d^4x_1 S(x_1',\mathbf{v}) \int d^4x_2' S(x_2',\mathbf{v})} \tag{2.15}$$

This form of the correlator was given first by Koonin [38] in 1977 and has since then been re-derived in various ways [9, 45].

Note that $g(\mathbf{v},\mathbf{r}_0)$ contains the emission Wigner density S only in a time integrated form. Unique extraction of S by correlation measurements is therefore not possible. Fortunately, for using correlations as a QGP signal this is also not necessary since delayed freeze-out can be detected as an enhancement of g in the outwards direction due to the source propagation properties that we discussed in the previous section.

For practical correlation analyses, one has to choose a model for g since the true emission Wigner densities S are unknown. A common choice is to use a Gaussian that has an enhancement in its outwards size,

$$g(\mathbf{v},\mathbf{r}_0) = \frac{1}{(4\pi)^{3/2} R_{\mathrm{out}} R_\perp^2} \exp\left(-\frac{r_{\mathrm{out}}^2}{4R_{\mathrm{out}}^2(\mathbf{v})} - \frac{r_{\mathrm{side}}^2 + r_{\mathrm{long}}^2}{4R_\perp^2(\mathbf{v})} \right) \tag{2.16}$$

Correlations from final-state Coulomb and strong interactions can then be simulated by folding this source function with the appropriate wavefunction. We will demonstrate this for Coulomb, classical Coulomb and strong interaction in the following chapters.

Chapter 3

The Quantum Correlator

Treating Coulomb and strong final-state interactions is straightforward once the wavefunction formalism (2.14) has been established. One just needs to solve the Schrödinger equation for the relative motion of the particle pair and choose a model for the source function. For the Coulomb case, solutions will be obtained in parabolic coordinates, whilst the partial-wave analysis for including strong interactions will be performed in spherical coordinates.

3.1 Correlations from Coulomb interaction

The effects of Coulomb interaction can be calculated quite easily as it is possible to construct an analytic solution for the continuous energy spectrum of the Schrödinger equation with Coulomb interaction,

$$\left(-\frac{\hbar^2}{2\mu}\nabla^2 + \frac{Z_1 Z_2 e^2}{r}\right)\psi(\mathbf{r}) = E\psi(\mathbf{r}) \tag{3.1}$$

This is the equation for the reduced system that is obtained after separating center-of-mass and relative motion using the the reduced mass parameter $\mu = m_1 m_2/(m_1 + m_2)$.

The next step is to choose a coordinate system in which separation of solutions becomes possible. Clearly, given the spherical symmetry of the problem, a separation approach in spherical coordinates seems to be most promising. Indeed, separation in spherical coordinates is possible and leads to an infinite series of partial Coulomb waves which are simultaneous eigenstates of energy and angular momentum. This partial wave decomposition will be useful later; for constructing the total Coulomb wavefunction numerically, however, separation in parabolic coordinates

$$\xi = r + z, \quad \eta = r - z, \quad \varphi = \arctan\left(\frac{y}{x}\right) \tag{3.2}$$

is more convenient as it immediately leads to a closed solution. We will just briefly review the solution as it can be found in quantum textbooks [40, 43]. The inverse transformation for parabolic coordinates is found to be

$$x = \sqrt{\xi\eta}\,\cos\varphi, \quad y = \sqrt{\xi\eta}\,\sin\varphi, \quad z = \frac{1}{2}(\xi - \eta) \tag{3.3}$$

After some algebra, the line element $(dl)^2$ expressed in terms of parabolic differential elements is:

$$(dl)^2 = \xi\eta(d\varphi)^2 + \left(\frac{\eta}{4\xi} + \frac{1}{4}\right)(d\eta)^2 + \left(\frac{\xi}{4\eta} + \frac{1}{4}\right)(d\xi)^2 \tag{3.4}$$

Parabolic coordinate trajectories are orthogonal. Therefore, the Laplacian can be easily obtained from the line element coefficients by applying Gauss's theorem [30]. The

Schrödinger equation then reads

$$\left[-\frac{\hbar^2}{2\mu}\left(\frac{4}{\xi+\eta}\right)\left(\frac{\partial}{\partial\xi}\xi\frac{\partial}{\partial\xi}+\frac{\partial}{\partial\eta}\eta\frac{\partial}{\partial\eta}+\frac{\xi+\eta}{4\eta\xi}\frac{\partial^2}{\partial\varphi^2}\right)+\frac{Z_1Z_2e^2}{(\xi+\eta)/2}\right]\psi=E\psi \qquad (3.5)$$

Separation of variables is now possible; due to the axial symmetry of the scattering problem, the wavefunction must be independent of ϕ. The separation ansatz

$$\psi_C = f_1(\xi)f_2(\eta) \qquad (3.6)$$

together with the constraint that for large distances the solution should asymptotically behave like a plane wave in the z-direction with momentum $q \equiv \sqrt{2\mu E}$ leads to the solution

$$\psi_C(\xi,\eta) = \Gamma(1+i\gamma)e^{-\pi\gamma/2}e^{iq(\xi-\eta)/2}F(-i\gamma|1|iq\eta), \qquad (3.7)$$

$$\gamma \equiv \frac{Z_aZ_be^2\mu}{\hbar q} \qquad (3.8)$$

where F is the confluent hypergeometric function. By folding $|\psi_C|^2$ with the source distribution function $g(q,r)$ the correlation function can be obtained numerically without any further difficulties.

3.2 Correlations from strong interactions

Strong interactions can be approximately included in the wavefunction formalism for both neutral and charged particles by making a partial-wave expansion. The phases of the partial waves can then be corrected according to experimentally tabulated strong interaction phase

shifts. Thus, the experimental phase shifts provide all information about the wavefunction for r outside the interaction range $\sim$ 1 fm. Inside the interaction range of the strong interaction, a different approach is needed. The question how the wavefunction can be modeled in this range will be discussed later.

3.2.1 Basic partial wave analysis

The partial-wave decomposition can be performed for both neutral and charged particles. For particles without Coulomb interaction, the original plane-wave solution can be expanded in terms of spherical Bessel functions j_l through the relation

$$\psi_{NC}(\mathbf{q},\mathbf{r}) \equiv e^{i\mathbf{q}\cdot\mathbf{r}} = e^{iqr\cos\theta} = \sum_{l=0}^{\infty}(2l+1)i^l j_l(qr)P_l(\cos\theta), \tag{3.9}$$

where P_l is the lth Legendre Polynomial. The corresponding expansion of the Coulomb wavefunction (3.7) in terms of spherical Coulomb partial waves has similar structure; it reads

$$\psi_C(\mathbf{q},\mathbf{r}) = \frac{1}{qr}\sum_{l=0}^{\infty}(2l+1)i^l e^{i\sigma_l}F_l(\gamma;qr)P_l(\cos\theta), \tag{3.10}$$

$$F_l(\gamma,qr) \equiv 2^l e^{-\pi\gamma/2}\frac{|\Gamma(l+1+i\gamma)|}{(2l+1)!}e^{iqr}(qr)^{l+1} \times F(l+1+i\gamma|2l+2|-2iqr), \tag{3.11}$$

$$\sigma_l \equiv \arg\Gamma(l+1+i\gamma). \tag{3.12}$$

A detailed derivation of these expansions can be found in Messiah [43] and other standard quantum textbooks.

For including strong interactions, the partial waves have to be decomposed into incoming and outgoing states $\phi_l^{(\pm)}$:

$$\psi(\mathbf{q},\mathbf{r}) = \sum_{l=0}^{\infty}(2l+1)i^l\phi_l(qr)P_l(\cos\theta), \tag{3.13}$$

$$\phi_l(qr) \equiv \phi_l^{(-)}(qr) + \phi_l^{(+)}(qr) \tag{3.14}$$

$$\phi_l^{(\pm)} \equiv \begin{cases} (j_l \mp in_l)/2 & \text{no-Coulomb} \\ e^{i\sigma_l}\left(F_l(\gamma;qr) \mp iG_l(\gamma;qr)\right)/2qr & \text{Coulomb} \end{cases} \tag{3.15}$$

The functions n_l (spherical Neumann function) and G_l (irregular Coulomb wavefunction) are solutions that are irregular at the origin; their exact definition can be taken from [43].

The phase of the outgoing wave $\phi_l^{(+)}$ is affected by the strong interaction. It is shifted by $2\delta_l$ where δ_l can be taken from experiment. Fortunately, correcting the phases of the first few partial waves is sufficient as phase shifts quickly go to zero for higher values of l. For the particle correlations investigated in this study, good accuracy is already reached by modifying s- and p-wave phases only.

The full solution that includes strong interactions is numerically obtained by constructing the wavefunction ψ without strong interaction and by replacing a finite number of outgoing partial waves with phase-shifted waves:

$$\psi_{\text{strong}} = \psi_{\text{no-strong}} + \sum_l \left[\phi_l^{(+)}e^{2i\delta_l} - \phi_l^{(+)}\right] \tag{3.16}$$

3.2.2 Handling spin flipping

If one of the scattering particles has spin, things become slightly more difficult as flipping of the spin may occur. In this case, the projection of the orbital angular momentum is no longer conserved in the interaction. The tabulated phase shifts then refer to total angular momentum eigenstates. On the other hand, the outgoing partial wave solutions are eigenstates of orbital angular momentum with $m_l = 0$. This can be seen immediately by rewriting the Legendre polynomials in the partial wave expansion in terms of spherical harmonics through the relation

$$P_l(\cos\theta) = \sqrt{4\pi/(2l+1)}\, Y_{l,m_l=0}(\theta,\phi) \tag{3.17}$$

One therefore has to transform the problem into a basis of total angular momentum eigenstates by using the machinery of angular momentum addition. Here, we will treat the special case that a spinless particle scatters off a spin 1/2 particle which is true for the $p\pi^+$ or pK^+ correlations that will be investigated later. The direct product of the orbital angular momentum eigenstate of the partial wave $|l = 1, m_l = 0\rangle$ with the spin $1/2$ state $|\uparrow\rangle$ gives contributions to two total angular momentum eigenstates $|j, m_j; l\rangle$:

$$\left|\frac{3}{2},\frac{1}{2};1\right\rangle = \sqrt{\frac{2}{3}}\,|1,0\rangle\,|\uparrow\rangle + \sqrt{\frac{1}{3}}\,|1,1\rangle\,|\downarrow\rangle \tag{3.18}$$

$$\left|\frac{1}{2},\frac{1}{2};1\right\rangle = -\sqrt{\frac{2}{3}}\,|1,1\rangle\,|\downarrow\rangle + \sqrt{\frac{1}{3}}\,|1,0\rangle\,|\uparrow\rangle \tag{3.19}$$

Solving for the initial state gives

$$|1,0\rangle\,|\uparrow\rangle = \sqrt{\frac{2}{3}}\left|\frac{3}{2},\frac{1}{2};1\right\rangle + \sqrt{\frac{1}{3}}\left|\frac{1}{2},\frac{1}{2};1\right\rangle \tag{3.20}$$

After phase-shifting the $J = 3/2$ part by $e^{2i\delta_{l,J=3/2}}$ and the $J = 1/2$ part by $e^{2i\delta_{l,J=1/2}}$ one can use equations (3.18) and (3.19) to write (3.20) again in terms of the spherical harmonics of the partial wave states:

$$\begin{aligned} e^{2i\delta_l}Y_{l=1,m=0} \;\rightsquigarrow\; & \left(\frac{2}{3}e^{2i\delta_{l,J=3/2}} + \frac{1}{3}e^{2i\delta_{l,J=1/2}}\right) Y_{l=1,m=0}\;|\uparrow\rangle \\ + \; & \left(\frac{\sqrt{2}}{3}e^{2i\delta_{l,J=3/2}} - \frac{\sqrt{2}}{3}e^{2i\delta_{l,J=1/2}}\right) Y_{l=1,m=1}\,|\downarrow\rangle \end{aligned} \tag{3.21}$$

3.2.3 Isospin rotation under a resonance

If two particles interact through a resonance, they can convert into different species as only the sum of the particles' isospin is conserved. As an example, the two-particle product state of Ξ^- and a π^+ can go through the Ξ^{0*} resonance and give either a $\Xi^-\pi^+$ or a $\Xi^0\pi^0$ pair. This effect can be calculated quantitatively by simply making an isospin decomposition of the incoming state. The $\Xi^-\pi^+$ contributes to two different isospin states, which are

$$\left|I = \frac{3}{2}, m_I = \frac{1}{2}\right\rangle = \sqrt{\frac{1}{3}}\,|\Xi^-\pi^+\rangle + \sqrt{\frac{2}{3}}\,|\Xi^0\pi^0\rangle \tag{3.22}$$

and its orthogonal state,

$$\left|I = \frac{1}{2}, m_I = \frac{1}{2}\right\rangle = -\sqrt{\frac{1}{3}}\,|\Xi^-\pi^+\rangle + \sqrt{\frac{2}{3}}\,|\Xi^0\pi^0\rangle \tag{3.23}$$

From this immediately follows

$$\begin{aligned} \left|\Xi^-\pi^+\right\rangle &= \left(\frac{1}{3}\left|\Xi^-\pi^+\right\rangle + \frac{\sqrt{2}}{3}\left|\Xi^0\pi^0\right\rangle\right)_{I=3/2} \\ &+ \left(\frac{2}{3}\left|\Xi^-\pi^+\right\rangle - \frac{\sqrt{2}}{3}\left|\Xi^0\pi^0\right\rangle\right)_{I=1/2} \end{aligned} \tag{3.24}$$

In the vicinity of the Ξ^{0*} resonance, the isospin dependent phase-shift for $I = 1/2; J = 3/2$ becomes quite large which results in a non-zero conversion amplitude from between $|\Xi^-\pi^+\rangle$ and $|\Xi^0\pi^0\rangle$.

The overall expression for the phase shifts becomes quite long as the Ξ particles also have spin 1/2. By combining Eq. (3.24) with eq. (3.21), one arrives at the result

$$\begin{aligned} \left|\phi_{l,\text{previous-incoming}}\right\rangle \equiv \quad & \left|\Xi^-\pi^+; l=1, m_l=0\right\rangle|\uparrow\rangle \rightsquigarrow \\ \left|\Xi^-\pi^+; l=1, m_l=0\right\rangle|\uparrow\rangle \quad & \left(\frac{2}{3}e^{2i\delta_{l,I=3/2,J=3/2}} + \frac{4}{9}e^{2i\delta_{l,I=1/2,J=3/2}}\right. \\ & \left. + \frac{1}{9}e^{2i\delta_{l,I=3/2,J=1/2}} + \frac{2}{9}e^{2i\delta_{l,I=1/2,J=1/2}}\right) \\ + \quad \left|\Xi^-\pi^+; l=1, m_l=1\right\rangle|\downarrow\rangle \quad & \left(\frac{\sqrt{2}}{9}e^{2i\delta_{l,I=3/2,J=3/2}} + \frac{2\sqrt{2}}{9}e^{2i\delta_{l,I=1/2,J=3/2}}\right. \\ & \left. - \frac{\sqrt{2}}{9}e^{2i\delta_{l,I=3/2,J=1/2}} - \frac{2\sqrt{2}}{9}e^{2i\delta_{l,I=1/2,J=1/2}}\right) \\ + \quad \left|\Xi^0\pi^0; l=1, m_l=0\right\rangle|\uparrow\rangle \quad & \left(\frac{2\sqrt{2}}{9}e^{2i\delta_{l,I=3/2,J=3/2}} - \frac{2\sqrt{2}}{9}e^{2i\delta_{l,I=1/2,J=3/2}}\right. \\ & \left. + \frac{\sqrt{2}}{9}e^{2i\delta_{l,I=3/2,J=1/2}} - \frac{\sqrt{2}}{9}e^{2i\delta_{l,I=1/2,J=1/2}}\right) \\ + \quad \left|\Xi^0\pi^0; l=1, m_l=1\right\rangle|\downarrow\rangle \quad & \left(\frac{2}{9}e^{2i\delta_{l,I=3/2,J=3/2}} - \frac{2}{9}e^{2i\delta_{l,I=1/2,J=3/2}}\right. \\ & \left. - \frac{2}{9}e^{2i\delta_{l,I=3/2,J=1/2}} + \frac{2}{9}e^{2i\delta_{l,I=1/2,J=1/2}}\right) \end{aligned} \tag{3.25}$$

One can clearly see that if all phase-shifts are zero the original incoming state is obtained. Furthermore, if the phase shifts do not depend on I or J, the interaction is becomes elastic and the other three components are not mixed in. Resonance phase shifts are modeled using the Breit-Wigner formula. The relativistic expression is

$$\begin{aligned} \tan\delta_l &= \frac{\Pi}{M_R^2 - M^2}, \\ \Pi &= \frac{q^3}{q_0^3}\frac{M_R}{M}\Pi_0, \\ \Pi_0 &= M_R\Gamma \ . \end{aligned} \tag{3.26}$$

Here, q_0 is the resonant momentum and Γ is the width of the resonance. The simpler non-relativistic Breit-Wigner formula,

$$\tan\delta_l = \frac{1}{2}\frac{q^{2l+1}}{q_0^{2l+1}}\frac{\Gamma_0}{M_0 - M} \ , \tag{3.27}$$

can be used if $M/M_R \sim 1$.

3.2.4 Constructing the wavefunction inside of the interaction range

For relative distances smaller than the range of the strong interaction $\sim$ 1 fm, the wavefunction is no longer a physical quantity since the hadrons no longer interact like two point particles. This is especially true for resonances where there is significant microscopic rearrangement of the quarks, e.g. $\pi + \pi \leftrightarrow \rho$. To avoid artifacts that originate from integrating over this unphysical region with high weight, one has to replace the wavefunction by a smooth function which has to be consistent with the phase-shifts of the outgoing waves.

For $r < \epsilon$ one can choose

$$|\psi(\mathbf{q},\mathbf{r})|^2 = |\psi_C(\mathbf{q},\mathbf{r})|^2 + W(\epsilon,q) \tag{3.28}$$

where ψ_C is the Coulomb wave and W is constant for all $r < \epsilon$. W cannot be chosen arbitrarily since the wavefunction and the change in the density of states are related to each other [31]. Consistency with these parameters requires that the following equation is fulfilled:

$$\begin{aligned}\Delta\frac{dN}{dq} = \sum_l \frac{(2l+1)}{\pi}\frac{d\delta_l}{dq} &= \frac{4\pi q^2}{(2\pi)^3}\int d^3r\ \left(|\psi(\mathbf{q},\mathbf{r})|^2 - |\psi_C(\mathbf{q},\mathbf{r})|^2\right) \\ &= \frac{4\pi q^2}{(2\pi)^3}\left[\frac{4\pi\epsilon^3}{3}W(\epsilon,q)\right. \\ &\quad \left. + \int_\epsilon^\infty dr\ r^2 \int_0^{2\pi} d\phi \int_{-1}^{1} d\cos\theta \left(|\psi(\mathbf{q},\mathbf{r})|^2 - |\psi_C(\mathbf{q},\mathbf{r})|^2\right)\right]\end{aligned} \tag{3.29}$$

After inserting the expansions (3.10) and (3.13) and applying the orthogonality relation for Legendre polynomials,

$$\int_{-1}^{1} dx\ P_l(x)P_m(x) = \frac{2}{(2l+1)}\delta_{lm}, \tag{3.30}$$

one finally obtains

$$\Delta\frac{dN}{dq} = \frac{2q^2\epsilon^3}{3\pi}W(\epsilon,q) + \frac{2}{\pi}\sum_l(2l+1)\int_\epsilon^\infty dr\ \left|\tilde{\phi}_l(qr,\gamma,\delta_l)\right|^2 - |F_l(qr,\gamma)|^2 \tag{3.31}$$

$$\tilde{\phi}_l \equiv F_l + \frac{1}{2}(e^{2i\delta_l} - 1)(F_l - iG_l) \tag{3.32}$$

Combining (3.31) and the phase-shift relation in (3.29), one can solve for W by evaluating phase-shift derivatives and integrals of the type

$$I_l(\epsilon, q, \delta_l) \equiv \int_\epsilon^\infty dr\, |\psi_l(qr, \gamma, \delta_l)|^2 \tag{3.33}$$

where ψ_l stands for either one of $\tilde{\phi}_l$ and F_l. In order to avoid a numerical evaluation of these integrals, one can rewrite them using the recursion relations of Coulomb wave-functions: Since ψ_l is an eigenstate of the radial part H_r of the Hamiltonian, it obeys the one-dimensional radial Schrödinger equation:

$$H_r\psi_l \equiv \left[-\frac{\hbar^2}{2\mu}\frac{\partial^2}{\partial r^2} + \frac{l(l+1)}{2\mu r^2} + \frac{Z_1 Z_2 \mu}{r}\right]\psi_l = E_l\psi_l = \frac{q^2}{2\mu}\psi_l \tag{3.34}$$

The trick for solving the integral (3.33) for a given state ψ_l with outgoing momentum q is to take a second state ψ_l' that has infinitesimally higher momentum $q' = q + dq$. Then,

$$(q'^2 - q^2)\Re\int_\epsilon^\infty dr\psi_l'^*\psi = 2\mu\Re\int_\epsilon^\infty dr\left[(H_r\psi_l'^*)\psi_l - \psi_l'^* H_r\psi_l\right] \tag{3.35}$$

In the limit $dq \to 0$, all r.h.s. terms except for those involving the differential operator cancel. After integrating by parts,

$$2qI_l(\epsilon, q, \delta_l) = \Re\left[\left(\frac{\partial}{\partial r}\frac{\partial\psi_l^*}{\partial q}\right)\psi_l - \frac{\partial\psi_l^*}{\partial q}\frac{\partial\psi_l}{\partial r}\right]_\epsilon^\infty . \tag{3.36}$$

Evaluation at the upper limit $r \rightarrow \infty$ is not necessary as it is canceled in the subtraction (3.31) of the two integral expressions for phase-shifted and non-phaseshifted waves. The lower limit can be evaluated numerically using recursion relations for Coulomb waves [1]. The explicit steps are quite lengthy and are shown in appendix A of this thesis.

Now that the integral I_l is known, one can calculate W using I_l and derivatives of the phase shifts, $\frac{d\delta_l}{dq}$. The strong interaction correction radius ϵ was set to $1fm$ for all simulations. The dependence of the correlator on the choice of ϵ is not significant as long as ϵ is significantly smaller than any characteristic dimension of the source.

Chapter 4

The Classical Coulomb Correlator

In the previous chapter, it was shown that Coulomb forces influence the correlation function through the distortion of the two-particle quantum wave function. However, if the relative momentum of the two particles is large, the De Broglie wavelength becomes small, and a classical description should be reasonable. In this chapter, we present the calculations for Coulomb-induced correlations using a purely classical treatment and compare with the analogous quantum treatment.

4.1 Derivation of the classical correlation weight

To determine the correlation weight, we can consider a source which emits particles of mass μ and momentum $\mathbf{q}_0$ at $\mathbf{r}_0$ according to a probability $S(\mathbf{r}_0, \mathbf{q}_0)$. If the particles are then deflected from their straight-line trajectories by a Coulomb potential, $V = k/r$, their

final momentum distribution is

$$\frac{dN}{d^3q} = \int d^3r_0 S(\mathbf{r}_0, \mathbf{q}_0) \left| \frac{d^3q_0}{d^3q} \right|. \tag{4.1}$$

Solving this problem represents a solution to the correlation problem as the motion of two particles under a central force reduces to a one-particle problem. The correlation function is the ratio of the spectra with and without the presence of the Coulomb potential.

$$C(\mathbf{q}) = \frac{dN/d^3q_0}{dN/d^3q}. \tag{4.2}$$

If S is independent of $\mathbf{q}_0$, or depends only on a constant of the motion, e.g., the energy, the $\mathbf{q}$ dependence is S disappears and one can express the correlation in a simple expression.

$$\begin{aligned} C(\mathbf{q}) &= \int d^3r_0\, g(\mathbf{r}_0) \left| \frac{d^3q_0}{d^3q} \right| \\ &= \int d^3r_0\, g(\mathbf{r}_0) \left| \frac{q_0^2\, dq_0\, \sin\theta_0\, d\theta_0\, d\phi_0}{q\, dq\, \sin\theta\, d\theta\, d\phi} \right|, \end{aligned} \tag{4.3}$$

where $g(\mathbf{r}_0)$ is a normalized distribution that represents the spatial shape in S. By comparing Eq. (4.3) with Eq. (2.14), one can see that the classical analog of the squared quantum relative wavefunction is $|d^3q_0/d^3q|$.

To play the role of the squared relative wave function, the Jacobian $|d^3q_0/d^3q|$ must be expressed in terms of the asymptotic momentum $\mathbf{q}$ and the initial spatial separation $\mathbf{r}_0$. Here, we will follow the derivation of [35] and derive an equivalent, though more compact, expression.

The solution involves finding the three components of $\mathbf{q_0}$. This can be accomplished using the three constants of motion. The first constant is energy,

$$\frac{q_0^2}{2\mu} + \frac{k}{r_0} = \frac{q^2}{2\mu} \Rightarrow |q_0| = \sqrt{q^2 - \frac{2\mu k}{|\mathbf{r_0}|}} \tag{4.4}$$

$$q_0^2\, dq_0 = \sqrt{1 - \frac{2\mu k}{|\mathbf{r_0}|\, q^2}}\, q^2\, dq \tag{4.5}$$

Other constants of motion are the eccentricity vector [24]

$$\epsilon = \frac{\mathbf{q} \times \mathbf{L}}{\mu k} + \frac{\mathbf{r}}{r} = \frac{\mathbf{q} \times (\mathbf{r} \times \mathbf{q})}{\mu k} + \frac{\mathbf{r}}{r} \tag{4.6}$$

and angular momentum $\mathbf{L}$.

To simplify the algebra, we choose a coordinate system where the particle is initially located on the positive z axis, and the momentum is confined to the xz plane.

$$\mathbf{q_0} = \begin{pmatrix} q_0 \sin\theta_0 \\ 0 \\ q_0 \cos\theta_0 \end{pmatrix} \qquad \mathbf{r_0} = \begin{pmatrix} 0 \\ 0 \\ r_0 \end{pmatrix} \tag{4.7}$$

$$\mathbf{q} = \begin{pmatrix} q \sin\theta \\ 0 \\ q \cos\theta \end{pmatrix} \qquad \mathbf{r}/r \overset{t\to\infty}{\approx} \begin{pmatrix} \sin\theta \\ 0 \\ \cos\theta \end{pmatrix} \tag{4.8}$$

Note that θ is the angle between *final* momentum $\mathbf{q}$ and the *initial* relative position vector $\mathbf{r}_0$. Equating the eccentricity vector, (4.6), for the time of emission and for very large times yields two conditions

$$\mu k + r_0\, q_0^2 \sin^2\theta_0 = \mu k \cos\theta + r_0 q\, q_0 \sin\theta \sin\theta_0 \ , \tag{4.9}$$

$$r_0\, q_0^2 \cos\theta_0 \sin\theta_0 = r_0\, q\, q_0 \cos\theta \sin\theta_0 - \mu k \sin\theta \ , \tag{4.10}$$

where the angular momentum is $q_0 r_0 \sin\theta_0$.

Solving for $\sin\theta_0$ and $\cos\theta_0$, respectively, we obtain

$$\sin\theta_0 = \frac{q}{2q_0}\left\{\sin\theta \pm \left[\sin^2\theta - 2\gamma(1-\cos\theta)\right]^{1/2}\right\}, \tag{4.11}$$

$$\begin{aligned}\cos\theta_0 &= \frac{q}{q_0}\cos\theta - \frac{\mu k}{r_0 q_0^2}\frac{\sin\theta}{\sin\theta_0} \\ &= \frac{\cos\theta}{(1-\gamma)^{1/2}} - \frac{\gamma\sin\theta}{2(1-\gamma)\sin\theta_0}\ .\end{aligned} \tag{4.12}$$

Although these expressions are redundant, it is convenient to retain both of them. Here, the abbreviation $\gamma = 2\mu k/q^2 r_0$ has been introduced for convenience. Note that there are two possible solutions which correspond to the fact that for any given final momentum **q** there are two different trajectories which pass through $\mathbf{r_0}$. Inserting (4.11) in (4.12) gives

$$\begin{aligned}\cos\theta_0 &= \frac{\cos\theta}{\sqrt{1-\gamma}} - \frac{\gamma\sin\theta\sqrt{1-\gamma}}{(1-\gamma)\left[\sin\theta \pm \sqrt{\sin^2\theta - 2\gamma(1-\cos\theta)}\right]} \\ &= \frac{\cos\theta}{\sqrt{1-\gamma}} - \frac{(1+\cos\theta) \mp \sqrt{(1+\cos\theta)^2 - 2\gamma\,(1+\cos\theta)}}{2\sqrt{1-\gamma}}.\end{aligned} \tag{4.13}$$

Finally, we differentiate with respect to cos to obtain

$$\frac{d\cos\theta_0}{d\cos\theta} = \frac{1}{2\sqrt{1-\gamma}} \pm \frac{1}{2\sqrt{1-\gamma}}\frac{1+\cos\theta-\gamma}{\sqrt{(1+\cos\theta-\gamma)^2-\gamma^2}}. \tag{4.14}$$

If the two charges are of the same sign, the potential is repulsive and γ is positive. The argument of the square root in Eq. (4.14) can then become negative which restricts the limits of θ, $(2\gamma - 1) < \cos\theta \leq 1$. This constraint represents the physical fact that a particle of a given energy whose initial position is at $\theta = 0$ can not be emitted with asymptotic

momentum at $\theta = \pi$ because of the deflection of the Coulomb force. We enforce this restriction with a step function,

$$\left|\frac{d\cos\theta_0}{d\cos\theta}\right|_{\pm} = \left|\frac{1}{2\sqrt{1-\gamma}}\left(1 \pm \frac{1+\cos\theta-\gamma}{\sqrt{(1+\cos\theta-\gamma)^2-\gamma^2}}\right)\right| \times \Theta(1+\cos\theta-2\gamma) \tag{4.15}$$

The "+" solution is always positive and the "−" solution is always negative, so absolute values can be taken easily, and by adding the two solutions, one obtains

$$\left|\frac{d\cos\theta_0}{d\cos\theta}\right|_{\text{tot}} = \frac{\Theta(1+\cos\theta-2\gamma)}{\sqrt{1-\gamma}} \frac{1+\cos\theta-\gamma}{\sqrt{(1+\cos\theta-\gamma)^2-\gamma^2}} \tag{4.16}$$

Although there is a singularity at $\cos\theta = -1+2\gamma$, the expression remains integrable. In fact, to see that this result is physical, one can check that the integral (4.16) over $\cos\theta$ yields $\int d\cos\theta_0 = 2$. Making the substitution $u = 1+\cos\theta-\gamma$ and replace the step function with the integration limits,

$$\begin{aligned}
\int_{-1}^{1} d\cos\theta \left|\frac{d\cos\theta_0}{d\cos\theta}\right|_{\text{tot}} &= \int_{\gamma}^{2-\gamma} \frac{1}{\sqrt{1-\gamma}} \frac{u\,du}{\sqrt{u^2-\gamma^2}} \\
&= \frac{1}{\sqrt{1-\gamma}} \int_{0}^{(2-\gamma)^2-\gamma^2} \frac{dv}{\sqrt{v}} \\
&= \frac{1}{\sqrt{1-\gamma}} \int_{0}^{2\sqrt{1-\gamma}} dw \\
&= 2
\end{aligned} \tag{4.17}$$

Combining this with equation (4.5) and the relation $d\phi_0 = d\phi$ which comes from an-

gular momentum conservation, we have as our final result for the Jacobian:

$$\begin{aligned}\left|\frac{d^3q_0}{d^3q}\right| &= \left|\frac{q_0^2\, dq_0\, d\cos\theta_0\, d\phi_0}{q^2\, dq\, d\cos\theta\, d\phi}\right| \\ &= \frac{1+\cos\theta-\gamma}{\sqrt{(1+\cos\theta-\gamma)^2-\gamma^2}}\,\Theta(1+\cos\theta-2\gamma)\end{aligned} \tag{4.18}$$

4.2 Numerical Evaluation

With the inspiration from the previous section, we can now apply the result of Eq. (4.18) by considering a simple Gaussian example for the source.

$$g(\mathbf{r}) = \frac{1}{(4\pi)^{3/2}R_{\rm out}R_\perp^2}\exp\left(-\frac{r_{\rm out}^2}{4R_{\rm out}^2}-\frac{r_{\rm side}^2+r_{\rm long}^2}{4R_\perp^2}\right) \tag{4.19}$$

The resulting integral is rather complicated and will be solved numerically using Monte Carlo techniques. Complications arise from the singularity in Eq. (4.18). This singularity can be eliminated by performing a transformation of variables as was done in Eq. (4.17) when checking the integrability of the Jacobian,

$$w = \sqrt{(1+\cos\theta-\gamma)^2-\gamma^2},\quad 0<w<2\sqrt{1-\gamma}. \tag{4.20}$$

The Monte Carlo integration can then be performed by choosing w with a uniform distribution, which would exactly account for the Jacobian.

However, choosing w according to a uniform distribution would not account for any

angular dependence coming from a lack of spherical symmetry in the source function, $g(\mathbf{r})$. Since w is defined in terms of the angle between $\mathbf{r}$ and $\mathbf{q}$, it is best to perform the Monte Carlo sampling in a rotated frame where $\mathbf{q}$ defines the z' axis as shown in Fig. 4.1.

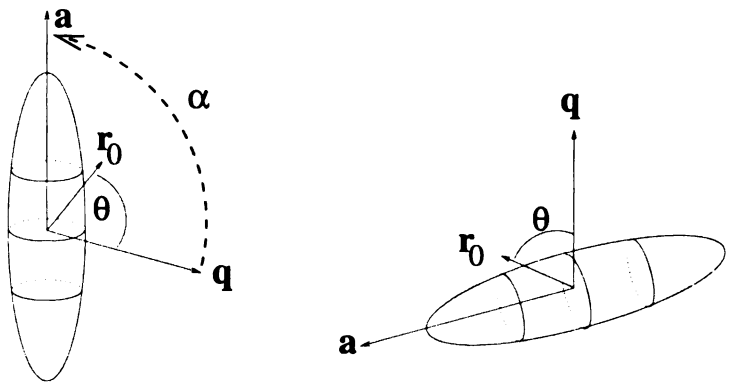

Figure 4.1: Rotation of the source frame for Monte Carlo integration

To understand the procedure it is best to re-express the integral in the new coordinate system:

$$\begin{aligned} C(q,\alpha) &= \int_0^\infty dr' r'^2 \int_{-1}^{1} d\cos\theta' \int_0^{2\pi} d\phi'\; g(R^{-1}(\alpha)\mathbf{r}') \\ &\times \frac{1+\cos\theta'-\gamma}{\sqrt{(1+cos\theta'-\gamma)^2-\gamma^2}}\,\Theta(1+\cos\theta'-2\gamma) \\ &= \int_{2\mu k/q^2}^\infty dr' r'^2 \int_0^{2\sqrt{1-\gamma}} dw \int_0^{2\pi} d\phi' \\ &\times g(R^{-1}(\alpha)\,\mathbf{r}'(r',w,\phi')) \end{aligned} \tag{4.21}$$

Here, R is the corresponding 3×3 rotation matrix, and α describes the direction of $\mathbf{q}$. Now that the integral over w is well-behaved, Monte Carlo integration is straight-forward.

We remember that, in general, for integrating a function f over an interval I, one gen-

erates a Monte Carlo rain of random numbers $\{x_i\}_{i=1..N}$ that are distributed according to a distribution function ρ that is non-zero all over I. Further, ρ has to be chosen in a way that the integral $\int \rho(x)\,dx$ exists. One defines $g \equiv f/\rho$. Then, by simply evaluating g at a large number of Monte Carlo points x_i and averaging over these values one obtains

$$\frac{\sum_{i=1}^{N} g(x_i)}{N} \overset{N\to\infty}{\longrightarrow} \langle g \rangle_\rho \equiv \frac{\int g(x)\rho(x)\,dx}{\int \rho(x)\,dx} = \frac{\int f(x)\,dx}{\int \rho(x)\,dx} \tag{4.22}$$

so that if $\int \rho(x)\,dx$ is known, $\int f(x)\,dx$ can be obtained by calculating $\langle g \rangle_\rho$. We now do exactly the same with our Monte Carlo problem. We write the integral (4.21) explicitly as

$$\begin{aligned} C(q,\alpha) &= \frac{1}{(4\pi)^{3/2} R_{\text{out}} R_\perp^2} \int_{2\mu k/q^2}^{\infty} dr' \int_0^{2\sqrt{1-\gamma}} dw \int_0^{2\pi} d\phi'\, r'^2 \exp\left(-\frac{r_{\text{out}}^2 + r_{\text{side}}^2 + r_{\text{long}}^2}{4R_{\text{out}}^2}\right) \\ &= \frac{R_{\text{out}}^2}{R_\perp^2} \int r'^2 dr' \int_0^2 dw \int_0^{2\pi} d\phi' \rho(\mathbf{r}')\,\Theta(1-\gamma)\,\Theta(2\sqrt{1-\gamma} - w) \\ &\quad \times \exp\left(-\frac{r_{\text{side}}^2 + r_{\text{long}}^2}{4R_\perp^2} + \frac{r_{\text{side}}^2 + r_{\text{long}}^2}{4R_{\text{out}}^2}\right) \qquad (4.23) \\ \rho(\mathbf{r}') &\equiv \frac{1}{(4\pi)^{3/2} R_{\text{out}}^3} \exp\left(-\frac{r'^2}{4R_{\text{out}}^2}\right) \qquad (4.24) \end{aligned}$$

Thus, the sampling function $\rho(\mathbf{r}')$ is simply a normalized spherically symmetric Gaussian based on R_{out}. The integral is then the weighted average,

$$C(q,\alpha) = \frac{R_{\text{out}}^2}{R_\perp^2} \left\langle \Theta(1-\gamma)\Theta(2\sqrt{1-\gamma} - w) \exp\left\{-\frac{r_{\text{side}}^2 + r_{\text{long}}^2}{4R_\perp^2} + \frac{r_{\text{side}}^2 + r_{\text{long}}^2}{4R_{\text{out}}^2}\right\} \right\rangle_\rho \tag{4.25}$$

This final expression can now be evaluated numerically. There are no problems with limited floating point accuracy as the values over which is W averaged have similar order

of magnitude. A more detailed underflow test gave a relative contribution of numerical errors to the final result of $< 10^{-8}$. Explicit data obtained from Monte Carlo simulation runs will be presented together with quantum mechanical results in the next chapter.

Chapter 5

Numerical Results and Discussion

5.1 Choosing particle pairs for correlation analyses

In principle, FSI correlation analyses can be performed with all observable particles. However, there are some issues that have to be dealt with that are less significant in identical particle HBT interferometry. Truly chaotic emission of the source is important for the success of any correlation analysis. For final-state correlations, this becomes a crucial issue as effects from Coulomb and strong interactions can be as low as 1%. Competing correlations must therefore be analyzed carefully.

There are mainly two mechanisms through which particles can acquire unwanted correlations before they enter the final state:

- If two particles share a quark-antiquark pair, there is a good chance that they are statistically correlated due to momentum conservation in pair creation. As an example, detecting a proton at high relative momentum enhances the probability that particles

containing $\bar{u}$ or $\bar{d}$ quarks are also detected in the same event at high relative momenta. Therefore, the use of particle pairs sharing a quark-antiquark pair for FSI correlation analyses is discouraged if the FSI peak is below 1 %.

- Correlations from jets and collective flow can also cause problems in a FSI correlation analysis. Careful construction of the correlator from events that have the same reaction plane should allow to minimize the effects of collective flow. Correlations from these two effects should be of the order of 0.5 %.

In general, experimental analyses should be restricted to ranges of $Q_{\text{inv}} \equiv 2q$ for which competing correlations are known to be significantly lower than the expected signal. For Coulomb correlations, which fall off as $1/Q_{\text{inv}}^2$, this typically limits Q_{inv} to below 200 MeV/c.

Further, it is important to remember that the wavefunction formalism is not covariant, so particle momenta in the center-of-mass frame should always be significantly lower than the corresponding particle masses. A truly covariant treatment of final-state interactions would be desirable. For small e^2, relativistic corrections can be crudely accounted for by altering the definition of the reduced mass,

$$\mu = \frac{E_1 E_2}{E_1 + E_2} \tag{5.1}$$

Fortunately, for the examples discussed in this study, the most important source information is hidden in the part of the correlator for which the invariant relative momentum Q_{inv} is still non-relativistic.

5.2 pK^+ correlations

Proton-kaon particle pairs are promising candidates for correlation analyses due to the fact that fewer particles originate from decays of long-lived resonances than in pion-based analyses. In the context of HBT interferometry, the advantage of using kaons instead of pions has already been discussed some time ago [26]. Further, pK^+ correlations do not have correlations from charge conservation in pair creation as uud and $u\bar{s}$ have no common quark-antiquark pair. The statistics for constructing the pK^+ correlation function should be available with current RHIC data sets.

Correlations of pK^+ particle pairs are dominated by Coulomb effects. Strong effects were included using phase shifts for $l = 0$ and $l = 1$ from experimental tables [18], but as it can be seen from Figure 5.1 they affect the correlator only moderately. In consistency with the findings of [14], the classical description of Coulomb effects is remarkably close to the quantum mechanical solution for large relative momenta Q_{inv}.

For measurements of the source shape, the dependence of the correlator on the angle between $\mathbf{q}$ and the outwards direction has to be analyzed. As already shown in eq. (4.5), the angle-averaged dependence of the correlator goes as

$$\frac{q_0^2 dq_0}{q^2 dq} = \sqrt{1 - \frac{2\mu k}{q^2 r_0}} \approx 1 - \frac{\mu k}{q^2 r} \tag{5.2}$$

Plotting $Q_{\text{inv}}^2(C(\mathbf{q}) - 1)$ instead of $C(\mathbf{q})$ should largely compensate this Q_{inv} dependence and emphasize the physical structure of the angular correlation plot. All of the following angular correlation plots will therefore employ this scaling.

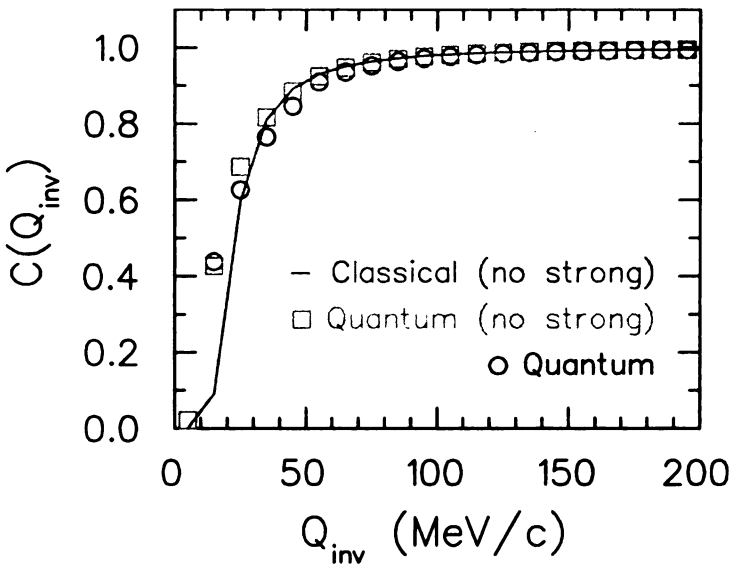

Figure 5.1: pK^+ correlations for a Gaussian source; $R_{\text{long}} = R_{\text{side}} = 4$ fm, $R_{\text{out}} = 8$ fm

The pK^+ angular correlation plot (fig. 5.2) shows again the good agreement with the classical approximation for large relative momenta. The minima at $\cos\theta = \pm 1$ are caused by the fact that the momenta of particles moving along the relative position axis are deflected away from this direction by repulsive Coulomb interaction.

The depth of the dips at $\cos\theta = \pm 1$ is proportional to $R^2_{\text{out}}/R^2_{\text{side}}$ for large values of Q_{inv}. Careful investigation of the classical correlator shows that for large q, where the correlation is confined to a small region where $\mathbf{q}$ is parallel to $\mathbf{r}_0$, the probability for the particles being separated by a given distance scales under a 90 degree rotation of the source as $R^3_{\text{out}}/R^3_{\text{side}}$ whilst the classical phase-space enhancement scales as $R_{\text{side}}/R_{\text{out}}$. In fact, the simulation for $R_{\text{out}}/R_{\text{side}} = 3$ gives an angular correlator that is nine times deeper for $\cos\theta = 1$ than for $\cos\theta = 0$. This favourable scaling behaviour of the angular dependence of the classical correlator shows that Coulomb induced correlations have strong

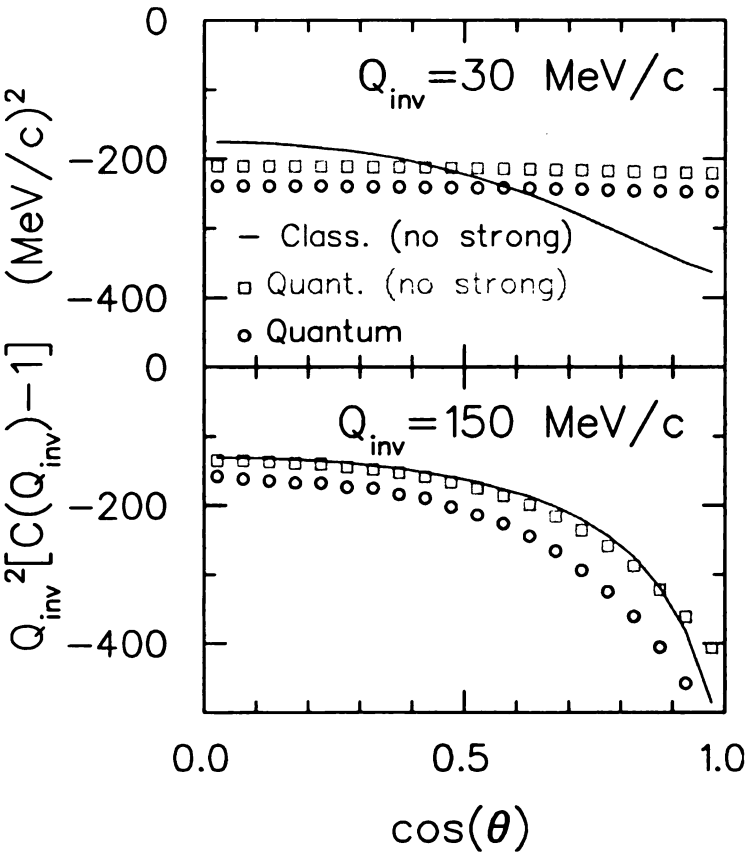

Figure 5.2: Angular pK^+ correlation; $R_{\text{long}} = R_{\text{side}} = 4$ fm, $R_{\text{out}} = 8$ fm

diagnostic power for resolving asymmetries of the source. For large Q_{inv}, the quantum results approach the classical result and thus have similar power to discern the shape of $g(\mathbf{r})$.

5.3 $p\pi^+$ correlations

So far, the strong interaction has contributed only minor corrections to a Coulomb-dominated correlator. We will now see that in the vicinity of a resonance, the strong interaction becomes the dominant factor and Coulomb effects become almost negligible. The

impact of the Δ^{++} resonance on correlations of $p\pi^+$ particle pairs will be investigated here as an example of correlation analyses in the vicinity of a resonance. Phase shifts for the $l = 0$ and $l = 1$ channels were again taken from experimental tables [18].

Near the resonant momentum, $Q_{\text{inv}} = 450$ MeV/c, the angular dependence of the correlator becomes quite large as one can see from Fig. 5.3. For resonant scattering, the

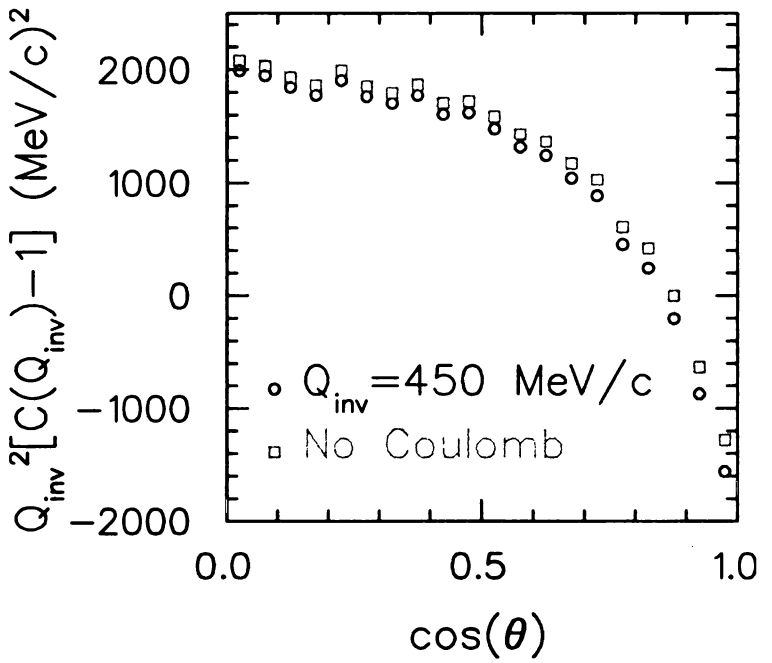

Figure 5.3: Angular dependence of the $p\pi^+$ correlator near the Δ^{++} resonance; $R_{\text{long}} = R_{\text{side}} = 4$ fm, $R_{\text{out}} = 8$ fm

angular dependence of the correlator arises due to shadowing in the forward direction. One can verify that shadowing is indeed the reason for the dip at $\cos\theta = \pm 1$ by running the correlation simulation for a greatly exaggerated scenario where the source is displaced by $Z_{\text{offset}} = 40$ fm in the direction of R_{out}. If shadowing is the real cause for the dip in the angular dependence graph, one can expect that for the displaced source this would result in a very narrow dip at $\cos\theta = -1$ where the particle first travels in the direction of its partner

and is then scattered. All other areas of the correlator should at most show small enhancements over unity that are proportional to $d\sigma/d\Omega$ as all scattered particles are deflected in some other direction and give a contribution to the correlator in this direction. Coulomb interaction has to be neglected since its long-range repulsive nature would modify the result significantly and therefore complicate the investigation of strong interaction effects.

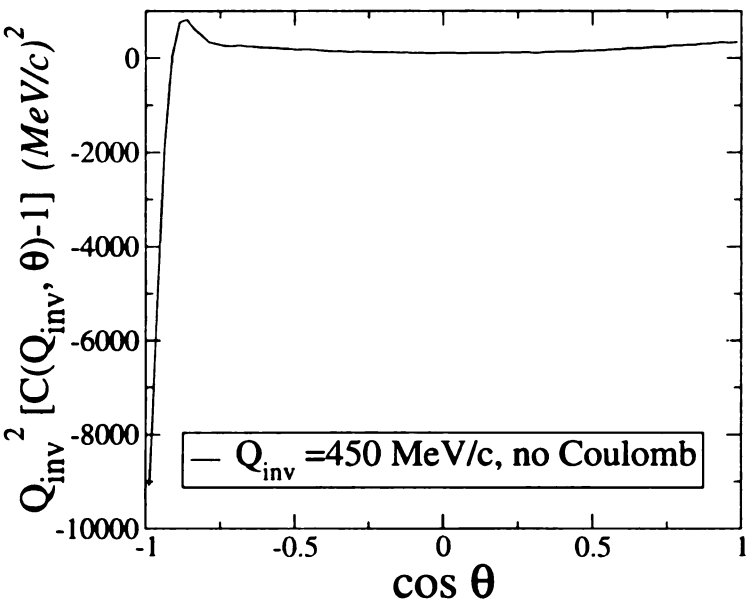

Figure 5.4: Shadowing by strong interaction near the resonance momentum; $R_{\text{long}} = R_{\text{side}} = R_{\text{out}} = 4$ fm; $Z_{\text{offset}} = 40$ fm

The numerical result of this demonstration run is displayed in figure 5.4. It is consistent with all our expectations and shows clearly that shadowing effects are the true physical reason for the dip in the angular part of the $p\pi^+$ correlator at resonant momentum. The small positive peak at $\cos\theta \approx -0.8$ results from diffraction.

5.4 $\Xi^-\pi^+$ correlations

As a last example we will discuss the resonant scattering of $\Xi^-\pi^+$ through the Ξ^{0*} resonance which also involves isospin rotation as described in section 3.2.3. The resonance resides at $Q_{\text{inv}} \approx 295$ MeV/c and gives an angular distribution that is again dominated by shadowing (see Fig. 5.5). A significant difference to the previous resonance is, however, that the resonance is very sharp and resides at low relative momentum which results in an especially clear peak in the correlator. Since the relevant structures are of the order of 10 % and above, they should be observable with moderate statistics.

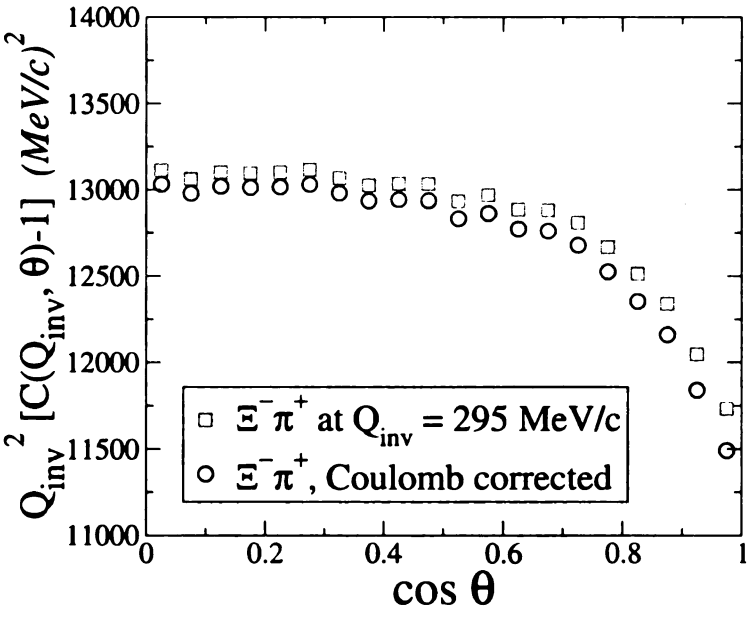

Figure 5.5: $\Xi^-\pi^+$ correlations at resonant momentum; $R_{\text{long}} = R_{\text{side}} = 4$ fm, $R_{\text{out}} = 8$ fm

Chapter 6

Conclusion and Outlook

Two-particle correlation functions provide tremendous information on the physical nature of the freeze-out state of a heavy ion collision. The three most important parameters that can be extracted from the correlations are the lifetime $\triangle\tau$ of the source as extracted from the ratio $R_{\rm out}/R_{\rm side}$, the average emission time $< \tau >$ that is obtained from $R_{\rm long}$, and the overall volume of the emitting region.

If a quark-gluon plasma is formed in the collision process and if the phase transition is of first order, it would have a large amount of latent heat. This would result in low pressure and a long lifetime [44, 54, 56] of the order $\sim 10 - 20$ fm/c. Particle emission should be continuous over the entire lifetime of the plasma.

The first results of HBT measurements at the Relativistic Heavy Ion Collider (RHIC) [6] were a real surprise for the heavy ion physics community as they showed nearly equal outwards and sidewards source sizes. This places an upper limit on the lifetime of the source of $\triangle\tau < 10$ fm/c which is significantly less than expected. Moreover, the average

emission times $\langle\tau\rangle$ were also unexpectedly small. The fact that none of the current dynamical models is able to match both the observed particle momentum spectra and these small HBT radii is referred to as the "HBT puzzle" [47, 56, 37]. There are two possible interpretations of these facts: either HBT measurements are unreliable for some unknown reason, or our picture of a relativistic heavy ion collision is incorrect.

The first interpretation can be probed by measuring source sizes through alternative methods. In this thesis, it was shown that non-identical particle correlations from final-state Coulomb and strong interactions carry important information on the source that allow the extraction of its size and lifetime and thus provide an alternative method. An article that has been submitted for publication [51] will summarize these results.

The HBT puzzle is challenging our models of the quark-gluon plasma. The fact that our models overpredict HBT radii could be caused by the mere non-existence of a QGP. Hydrodynamical models are based on minimum-increase-in-entropy propagation, yet they overpredict the measured HBT radii and the measured per-particle entropy. This would indicate that the true initial state had much lower entropy and could not have been a quark-gluon plasma. On the other hand, other observables like the charge balance functions that will be discussed in the following part of this thesis seem to indicate that a QGP might indeed have been formed in RHIC Au+Au collisions.

Intensive work will be required in order to finally resolve all these issues and to give a final answer on the existence and nature of the quark-gluon plasma.

Part II

Modeling Balance Functions in Heavy Ion Collisions

Chapter 7

The Balance Function Formalism

It was already mentioned in the first part of this thesis that the constraints of charge conservation in pair creation cause significant statistical correlations in momentum space between particles and their balancing antiparticles. Whilst these correlations are harmful in the context of two-particle FSI source measurements which rely on chaotic emission, they may carry important information on the timescale of pair creation. Charge balance functions were introduced as a new observable [13] that allows to quantify such correlations. The strong sensitivity of these functions with respect to the timing of hadronization makes them good candidates for a QGP signal.

The current chapter will give a brief overview of the balance function approach whilst the following chapter will address specific issues that are relevant for Monte-Carlo simulations of balance functions.

7.1 Introduction

The canonical picture of a relativistic heavy ion collision that forms a QGP assumes that the plasma phase would be quite long-lived as its internal pressure would be low due to the high amount of latent heat stored in the plasma. As the plasma expands and cools, it returns to ordinary hadronic matter through a phase transition that might be of first order [33, 34]. This phase transition is accompanied by a massive increase in the number of quark-antiquark pairs as the entropy stored in the plasma is converted to mesons. Since gluons carry no charge, and hadrons contain at least two quarks, most of the electric charge, strangeness and baryon number is therefore produced at a late stage of the collision if a QGP intermediate state exists. The timing of hadronization is the most obvious difference between a collision that involves a QGP and a collision that involves just purely hadronic intermediate states and that is characterized by early hadronization $\sim 1fm/c$.

If charges are created early, they can separate further in rapidity due to the collective expansion of the collision process. A simple toy model can show how drastic this effect should be: In a Bjorken expansion model, the rapidity gradient along the beam axis is approximately given by $1/\tau$. If quarks separate by $0.5fm$ at a time of $0.5fm/c$, their final difference in rapidity should therefore be of the order of magnitude of 1. On the other hand, if late hadronization due to a QGP intermediate state occurs at $\tau \sim 5fm$, the difference in rapidity of a quark-antiquark pair initially created at relative distance of $0.5fm$ would be just ~ 0.1.

The purpose of balance functions is to identify a meson's balancing charge and to mea-

sure its difference in rapidity on a statistical basis. One defines the balance function as

$$B(P_2|P_1) \equiv \frac{1}{2}\left\{\frac{N_{+-}(P_1,P_2) - N_{++}(P_1,P_2)}{N_+(P_1)} + \frac{N_{-+}(P_1,P_2) - N_{--}(P_1,P_2)}{N_-(P_1)}.\right\} \quad (7.1)$$

Here, $N_{+-}(P_1, P_2)$ is the number of events where a positive particle of a given species was observed in the bin P_1 and its balancing particle was observed in the bin P_2. There are many possible binning criteria, but we will focus on relative rapidity in this thesis. Also note that the counting for $N_\pm$ does not necessarily have to refer to electric charge. The balanced "charge" could for just as well be strangeness, baryon number, or isospin I_3. One can construct balance functions using all positive and all negative, all strange and all antistrange particles, or with particle and antiparticles of a given species, e.g. $\pi^+\pi^-$.

The normalization of the balance function would be unity if the colliding nuclei had no surplus charges and the detector had an acceptance of unity, i.e. all particles were detected. For a lower detector acceptance, the balance function will sum to the fraction of particles carrying the globally conserved charge that is actually detected. Furthermore, if the balance function is constructed using a subset of particles, e.g. K^+K^-, the normalization would be reduced since the balancing charge might be carried by another particle.

7.2 Balance functions as a QGP signal

There is an especially interesting class of balance functions that uses the specific binning that P_1 should be the detection of any particle in the experimental acceptance, and P_2 should be the detection of a particle with relative rapidity Δy. The properties of this specific

charge balance function have been investigated in several papers [13, 46, 32, 49] and have also been measured at RHIC by STAR [4].

The expectation is that if a QGP is formed in a relativistic heavy ion collision, the peak of the balance function at $\Delta y = 0$ should be much narrower than the peak of a balance function of a pp collision. Moreover, the peak should also become narrower with increasing centrality of the Au+Au collision the higher temperatures would result in an enhancement to the lifetime of the QGP and an additional delay in emission time. For a purely hadronic collision scenario, emission times should not change and the balance function should not become narrower with increasing collision centrality. Simulations using hadronic cascade models have confirmed this expectation. Figure 7.1 shows the balance function as obtained from the hadronic cascade models HIJING and GROMIT which simulate immediate hadronization according to pp phenomenology.

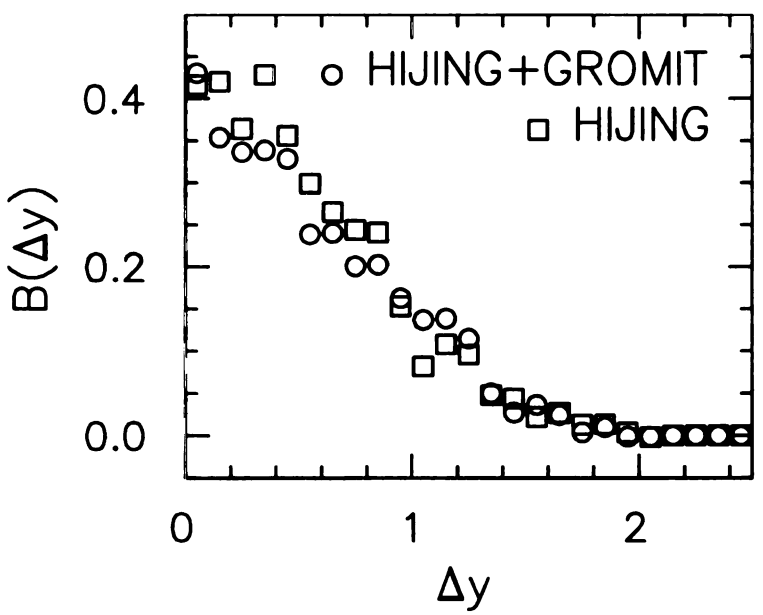

Figure 7.1: Balance functions obtained from hadronic cascade models

A first measurement of balance functions at RHIC has been performed by the STAR collaboration [4]. It was found that the balance function becomes narrower by approximately 20% for central collisions (see fig. 7.2) whilst for peripheral collisions it approaches the width that is predicted by hadronic models.

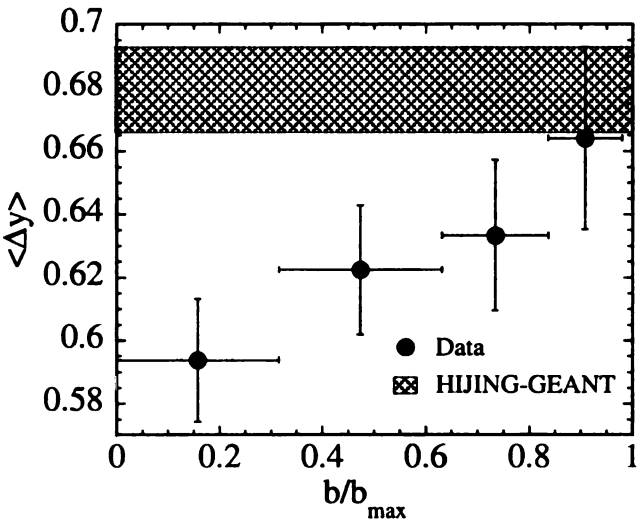

Figure 7.2: Narrowing of the pion balance function with increasing centrality of the collision as measured at STAR

The theoretical modeling of balance functions for any kind of emission scenario is quite complex since one has to simulate particle multiplicities and momenta, and disturbing effects like the unbalanced charges of the two nuclei [49], the limited detector acceptance and effects from HBT correlations [32] have to be accounted for.

A problem in balance function simulations is that the observed particle multiplicities have to be modeled in a way that the constraint of charge conservation is observed. Models that just create particle-antiparticle pairs neglect the possibility that the balancing charge of a particle may actually be spread over several other particles due to charge mixing and

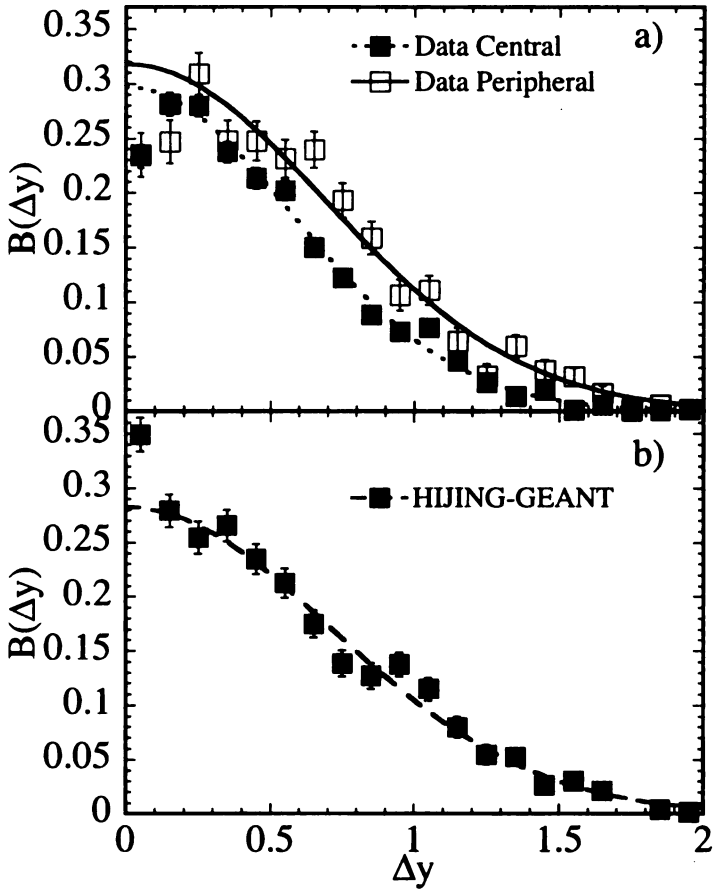

Figure 7.3: Balance functions for charged pions as measured at STAR in comparison to theoretical data from hadronic cascade models

chemical equilibration at an early stage of the collision. Therefore, we have developed a new thermal model for generating particle multiplicities which accounts for charge mixing whilst charge conservation is still strictly enforced. We will discuss the theory, implementation details and present preliminary results of this model in the following chapters.

Chapter 8

Modeling Particle Multiplicities

Particle multiplicities generated according to a thermal model using a canonical ensemble have been shown to reflect observed multiplicities quite well [16]. Local charge conservation can be modeled by providing for each particle a balancing antiparticle, so for instance every π^+ would be accompanied by production of a π^-. However, this simple model does not account for the effects of charge mixing in the process of chemical equilibration. As an example, the a K^+ could be balanced by a $\bar{p}$ and a Λ. To include such effects, a new algorithm was developed in order to simulate charge-conserving particle creation according to a canonical ensemble.

8.1 Recursion relations for partition functions

Let us consider a system which consists of A particles that have a total charge (baryon number, strangeness, isospin I_3 etc) of $\vec{Q}$. Assuming that there are Γ different species of particles with charge $\vec{q}_k$ and a single particle partition function ω_k, the total partition

function for A particles is

$$Z_A(\vec{Q}) = \sum_{\left\langle \begin{array}{l} \sum_k n_k \vec{q}_k = \vec{Q}, \\ \sum_k n_k a_k = A \end{array} \right\rangle} \prod_{k=1}^{\Gamma} \frac{(\omega_k)^{n_k}}{n_k!} \quad . \tag{8.1}$$

The number a_k must be a positive quantity for all particles. For calculating the total partition function $Z = \sum_a Z_a$, the assignment of a_k becomes arbitrary. We will choose to assign $a_k = 1$ to all particle types that are sufficiently long-lived to reach the detector, and $a_k = 2$ to extremely short-lived particles. With this choice, $\sum_k a_k$ roughly reflects the number of particles that are created, though some unstable species might have some 3-body decay channels.

Expression (8.1) is almost useless for practical purposes since solving the combinatoric problem of finding all possible n_k has exponential complexity. However, by using recursion relations and caching all results in memory, the computational effort required for solving the problem can be drastically reduced [19, 23, 20, 52].

The recursion relations are easily obtained by inserting a factor of 1 and rewriting the expression as

$$Z_A(\vec{Q}) = \sum_{\left\langle \begin{array}{l} \sum_k n_k \vec{q}_k = \vec{Q}, \\ \sum_k n_k a_k = A \end{array} \right\rangle} \underbrace{\left(\sum_{k'} \frac{n_{k'} a_{k'}}{A} \right)}_{=1} \prod_{k=1}^{\Gamma} \frac{(\omega_k)^{n_k}}{n_k!} \tag{8.2}$$

$$= \sum_{k'} \frac{\omega_{k'} a_{k'}}{A} \sum_{\left\langle \begin{array}{l} \sum_k n_k \vec{q}_k = \vec{Q}, \\ \sum_k n_k a_k = A \end{array} \right\rangle} \frac{\omega_{k'}^{n_{k'}-1}}{(n_{k'}-1)!} \prod_{\substack{k=1 \\ k \neq k'}}^{\Gamma} \frac{\omega_k^{n_k}}{n_k!} \tag{8.3}$$

$$= \sum_{k'} \frac{\omega_{k'} a_{k'}}{A} \sum_{\left\langle \begin{array}{l} \sum_k n_k \vec{q}_k = \vec{Q} - \vec{q_k}, \\ \sum_k n_k a_k = A - a_k \end{array} \right\rangle} \prod_{k=1}^{\Gamma} \frac{\omega_k^{n_k}}{n_k!} \tag{8.4}$$

$$= \sum_{k'} \frac{\omega_{k'} a_{k'}}{A} Z_{A-a_k}(\vec{Q} - \vec{q_k}) \tag{8.5}$$

This simple recursion relation can be used to build a partition function table in memory for a relatively high number of particles ($A \sim 50$). However, memory and CPU time consumption can be tremendous if poorly optimized code is used. Since algorithmic optimization is crucial for generating partition functions for larger A on workstation-class hardware, the specific optimization techniques employed in the final C++ implementation are discussed more in detail in the next section.

8.2 Optimization issues

One of the key issues in creating an efficient implementation of the recursion relations is the reduction of the number of partition functions actually calculated. Quite often, there is no combination of charges so that $\sum_k n_k \vec{q}_k = \vec{Q} - \vec{q_{k'}}$ and $\sum_k n_k a_k = A - a_{k'}$. In these cases, the contribution of $Z_{A-a_{k'}}(\vec{Q} - \vec{q_{k'}})$ in 8.5 is zero. Since the number of zero values by far exceeds the number of non-zero values, an efficient implementation must avoid calculating and storing zero-value contributions.

Therefore, the first step toward an optimized implementation involves changing from the original recursive algorithm to an algorithm that starts at the bottom ($A = 0$) and works its way up to the top ($A = A_{\text{max}}$) by only calculating the non-zero partition functions. Its basic working principle can be described by the following pseudo-code:

```
Allocate and assign Z[A=0](Q=0) = 1;
Run for A from 0 to A_MAX
  For (every non-zero value Z[A](Q) in memory)
     For (every particle species k) {
        Allocate Z[A+a[k]](Q + q[k]) in memory if necessary;
        Make the respective contribution to Z[A+a[k]](Q + q[k]);
     }
```

In comparison to an algorithm that calculates all values of Z for the full charge range that could possibly be combined from A particles, the requirements in CPU time are reduced by a factor ~ 50.

Results should be stored in memory in a way that allows iterating the non-zero values of $Z_A(\vec{Q})$ efficiently whilst providing fast access to the individual values. The C++ implementation uses an array of STL template classes of type `map<charge,double>` which map a user-defined `charge` class to a `double` that holds the non-zero partition function value. Iterating through all non-zero values using STL container iterators is efficient and easy. As no zero values are stored in memory, total memory consumption is reduced by several orders of magnitude compared to an implementation that relies on arrays. Data access for a single item is of complexity $\mathcal{O}(\log n)$ which is acceptable even for intensive Monte Carlo simulations.

The fact that particle and antiparticle partition functions are always identical allows further optimization by skipping the calculation of $Z(-\vec{Q})$ and simply returning $Z(\vec{Q})$. However, contributions to partition functions that cross the axis of charge symmetry can lead to double-counting and finally wrong results if the optimization is not done carefully. The implementation of charge-anticharge symmetry brings a performance boost of $\sim 70\%$ and cuts memory consumption by another 40%.

The C++ implementation that was developed in the context of this thesis takes care of three charge conservation constraints: Isospin I_3, baryon number and strangeness. The particle species that were included for the simulation are listed in appendix B. The calculation of the partition function up to $A = 55$ using the optimized C++ implementation took about 20 minutes and consumed 950 MB of memory on an Intel-based 2 GHz system.

It can be clearly seen that without the optimization techniques described above which all together reduced memory consumption by a factor ~ 10, the calculation of the partition function for such high values of A would not be possible on a workstation-class computer.

8.3 Monte-Carlo generation of particles

Particle multiplicities are obtained from the constructed partition functions using the following algorithm: First, the total particle number A is chosen according to $Z_A(\vec{Q} = 0)$. This is physically correct as the total partition function of a charge-neutral system with an arbitrary number of particles is simply

$$Z(\vec{Q} = 0) = \sum_A Z_A(\vec{Q} = 0) \; . \tag{8.6}$$

where Z_A gives the weight of the A-particle state. When the particle number A has been determined, one can Monte-Carlo the individual particles:

1. A particle of species k is chosen proportional to the weight $\frac{a_k \omega_k}{A} Z_{A-a_k}(\vec{Q} - \vec{q_k})$

2. A is replaced by $A - a_k$, and $\vec{Q}$ is replaced by $\vec{Q} - \vec{q_k}$, then step 1 is repeated until $A = 0$ is reached.

It will now be shown formally that this algorithm chooses every particle configuration with a probability that is proportional to its contribution to the partition function $Z_A(\vec{Q})$. Again, we denote the charge vectors for the different particle species as $\vec{q_k}$. Note that these charge vectors are not always linearly independent. A set of particles will be referred to as $\{k_1, \ldots, k_N\}$ where the i-th particle is of type k_i, $1 \leq i \leq N$. Note that this definition is sensitive to the ordering of the particles. For a given value of total charge $\vec{Q}$ and associated number A we will call the set $\{k_1, k_2, \ldots, k_N\}$ a *path* to $(\vec{Q}, A)$ and write $\mathcal{D}_A^N(\{k_1, \ldots, k_N\}; \vec{Q})$ if

$$\vec{Q} = \sum_{i=1}^{N} \vec{q}_{k_i} \text{ and } A = \sum_{i=1}^{N} a_{k_i}. \tag{8.7}$$

Note that for fixed $(\vec{Q}, A)$ there is a large number of possible paths, and not all paths necessarily have the same number of particles N.

Let us now define the *path contribution* $\mathcal{Z}$ for a given path $\mathcal{D}_A^N(\{k_1, \ldots, k_N\}; \vec{Q})$ as

$$\mathcal{Z}(\mathcal{D}_A^N(\{k_1, \ldots, k_N\}; \vec{Q})) \equiv \prod_{i=1}^{N} \frac{\omega_{k_i} a_{k_i}}{\sum_{j=1}^{i} a_{k_j}}. \tag{8.8}$$

The partition function $Z_A(\vec{Q})$ is the sum over the path contributions of all paths to $(\vec{Q}, A)$. This can be shown by analyzing the recursion relations of the new function

$$\tilde{Z}_A(\vec{Q}) \equiv \sum_N \sum_{\substack{\text{all paths} \\ \mathcal{D}_A^N(\{k_1,\ldots,k_N\};\vec{Q})}} \mathcal{Z}(\mathcal{D}_A^N(\{k_1,\ldots,k_N)\};\vec{Q})) \tag{8.9}$$

It is possible to factorize out the contribution of the last particle of this path:

$$\tilde{Z}_A(\vec{Q}) = \sum_N \sum_{\substack{\text{all paths} \\ \mathcal{D}_A^N(\{k_1,\ldots,k_N\};\vec{Q})}} \prod_{i=1}^{N} \frac{\omega_{k_i} a_{k_i}}{\sum_{j=1}^{i} a_{k_j}} \tag{8.10}$$

$$= \sum_{k'} \sum_N \sum_{\substack{\text{all paths} \\ \mathcal{D}_{A-a_{k'}}^{N-1}(\{k_1,\ldots,k_{N-1}\};\vec{Q}-\vec{q}_{k'})}} \prod_{i=1}^{N} \frac{\omega_k a_{k_i}}{\sum_{j=1}^{i} a_{k_j}} \frac{\omega_{k'} a_{k'}}{A} \tag{8.11}$$

$$= \sum_{k'} \frac{a_{k'}\omega_{k'}}{A} \tilde{Z}_{A-a_{k'}}(\vec{Q}-\vec{q}_{k'}) \tag{8.12}$$

We see that $\tilde{Z}_A$ obeys the same recursion relations as Z_A. Since Z_A is well-defined by the recursion relations and the initial value $Z_0(0) = 1$, the new object $\tilde{Z}_A$ must be equal to Z_A. Thus, the partition function $Z_A(\vec{Q})$ is really the sum over the path contributions $\mathcal{Z}(\mathcal{D}_A^N)$ of all paths to $(\vec{Q}, A)$.

Now we calculate the probability that the algorithm will select a specific path $\mathcal{D}_A^N(\{k_1,\ldots,k_N\},\vec{Q})$ that has a path contribution of $\mathcal{Z}(\mathcal{D})$. Starting at $(\vec{Q}=0, A)$, the probability to select the particle species k_N for the last (N-th) particle is

$$\mathcal{P}(k_N) = \frac{\omega_{k_N} a_{k_N}}{A} \frac{Z_{A-a_{k_N}}(\vec{Q}-\vec{q}_N)}{Z_A(\vec{Q}=0)}. \tag{8.13}$$

Similarly, the probability to obtain the particle species k_N for the last and k_{N-1} for the next particle is

$$\mathcal{P}(k_N, k_{N-1}) = \frac{\omega_{k_N} a_{k_N}}{A} \frac{\omega_{k_{(N-1)}} a_{k_{(N-1)}}}{A - a_{k_N}} \frac{Z_{A-a_{k_N}}(\vec{Q} - \vec{q}_N)}{Z_A(\vec{Q} = 0)} \frac{Z_{A-a_{k_N}-a_{k_{(N-1)}}}(\vec{Q} - \vec{q}_{k_N} - \vec{q}_{k_{N-1}})}{Z_{A-a_{k_N}}(\vec{Q} - \vec{q}_N)} \tag{8.14}$$

One can see that the partition function $Z_{A-a_{k_N}}(\vec{Q} - \vec{q}_{k_N})$ cancels. Iteratively one obtains for the probability to choose a given path $\mathcal{D}_A^N(\{k_1, \ldots, k_N\}, \vec{Q})$ the value

$$\mathcal{P}(\mathcal{D}_A^N(\{k_1, \ldots, k_N\}, \vec{Q})) = \frac{\mathcal{Z}(\mathcal{D}_A^N(\{k_1, \ldots, k_N\}, \vec{Q}))}{Z_A(\vec{Q} = 0)}, \tag{8.15}$$

which is proportional to the physical weight that this path contributes to the partition function $Z_A(\vec{Q} = 0)$. Thus, the algorithm chooses paths according to the definition of $\mathcal{Z}$ in Eq. (8.8) which is consistent with the contribution of the configuration to the partition function.

Chapter 9

Results and Conclusion

9.1 Constructing the balance function

In this section, we will briefly sketch the other steps that are necessary for constructing balance functions from the thermal model that was discussed in the previous chapter. After generating particle multiplicities according to the described Monte Carlo procedure at a chemical freeze-out temperature of $T_\mu = 175$ MeV, the particle momenta in the source frame are assigned according to a thermal distribution at lower kinetic temperature $T_k = 120$ MeV which is the hadronic decoupling temperature measured at RHIC. The thermally generated particle multiplicities contain a significant amount of very unstable resonances that decay within a short period of time. This is accounted for by an algorithm that performs decays according to a list of known particle decay channels. Decay products are assigned momenta such that total momentum is conserved and the momentum correlations resulting from decays are reflected accurately.

Finally, a center-of-mass frame for the point-like source is chosen according to a blast-wave description at $T_{\text{blast}} = 120$ MeV, and all particles from a given source are boosted into that frame. Our specific choice of a blast-wave model is such that sources are assumed to be uniformly distributed in the transverse direction up to a maximum radius R,

$$\frac{dN}{r\,dr} = \begin{cases} \text{constant} & \text{for } r < R \\ 0 & \text{for } r > R \end{cases} \tag{9.1}$$

The transverse rapidities are assumed to increase linearly with r,

$$y_{\text{trans}} = \frac{r}{R} y_{\text{trans,max}} \tag{9.2}$$

Longitudinal rapidities are chosen randomly between $y = +2$ and $y = -2$.

After boosting the source to the frame according to the blast-wave model, particle pair interactions are neglected for simplicity. Interdomain correlations [50], i.e. correlations arising from long-range Coulomb interaction between particles from different sources have also been omitted in these simulations. The acceptance of the STAR detector has been modeled for the (pseudo)rapidity range of $-1 < \eta < 1$.

The thermally generated balance function of identified pions resulting from this simulation procedure shows good agreement to the actual STAR data as one can see in fig. 9.1.

9.2 Conclusion

Balance functions were introduced in order to obtain information on the timing of particle generation in relativistic heavy ion collisions. Although the formalism is still very young,

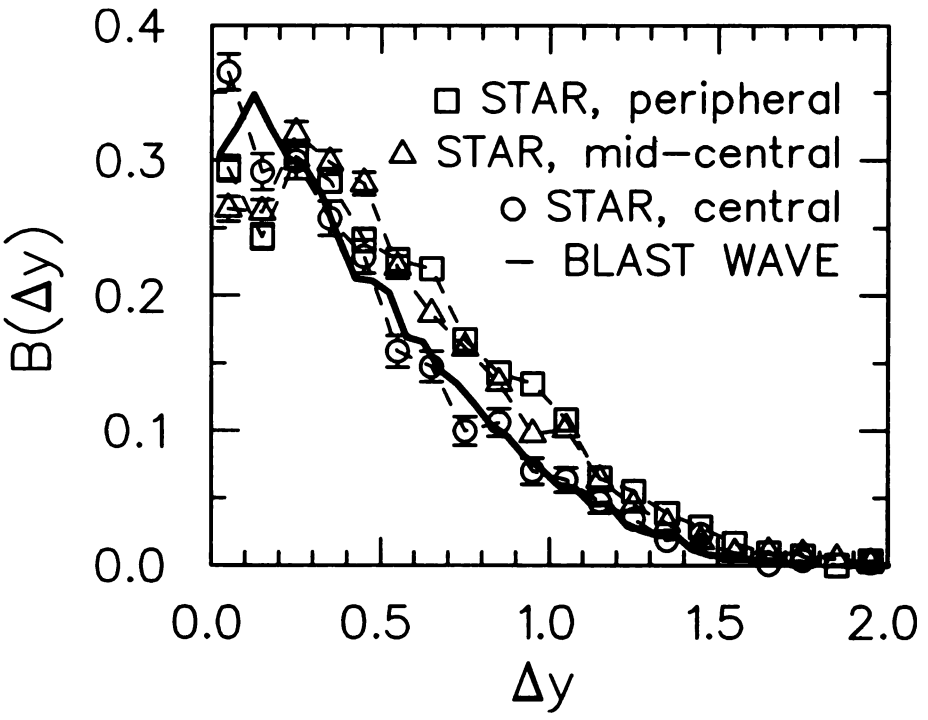

Figure 9.1: Thermally modeled balance function of identified pions in comparison to STAR measurements

balance functions seem to be already quite well-understood given the good agreement of theoretical predictions and actual STAR balance data. However, there are still aspects that have to be investigated deeper before the balance function can actually be called a a "QGP signal". Aspects that may affect the broadening of the balance functions like interdomain interactions have to be examined carefully in order to fully understand the width balance function in a nearly model-independent fashion.

Once all these issues have been resolved, it should be possible to clearly state whether or not the observed narrowing of the balance function with increasing collision centrality can be seen as a signal for the formation of a QGP. At the moment, balance functions can be seen as promising observables for the observation of a quark-gluon plasma.

APPENDICES

Appendix A

Recursion Relations for Coulomb Waves

A.1 Transformation to natural coordinates

Let $D := \{(r,q) \in \mathbb{R}^2 \mid q \neq 0\}$ and let $w : D \to \mathbb{R}^2$ be the coordinate transformation defined by

$$\begin{pmatrix} r \\ q \end{pmatrix} \mapsto \begin{pmatrix} \frac{me^2}{q} \\ qr \end{pmatrix}$$

Let $u : \mathbb{R}^2 \to \mathbb{C}$ be some complex function, and $\tilde{u} : M \to \mathbb{C}$ the function induced on M by the coordinate transformation, $\tilde{u} := u \circ w$.

From the chain rule,

$$\begin{aligned} d\tilde{u} &= du \circ dw \\ &= \left(\frac{\partial u}{\partial \eta}, \frac{\partial u}{\partial \rho}\right) \begin{pmatrix} 0 & me^2/q^2 \\ q & r \end{pmatrix} \end{aligned}$$

$$= \left(q\frac{\partial u}{\partial \rho}, -\frac{me^2}{q^2}\frac{\partial u}{\partial \eta} + r\frac{\partial u}{\partial \rho} \right)$$
$$= \left(\frac{\partial \tilde{u}}{\partial r}, \frac{\partial \tilde{u}}{\partial q} \right)$$

A.2 Evaluation of Eq. (3.36)

Let now $u_L : \mathbb{R} \to \mathbb{C}$ be a solution to the "Coulomb wave" differential equation

$$\frac{d^2}{d\rho^2} w + \left[1 - \frac{2\eta}{\rho} - \frac{L(L+1)}{\rho^2} \right] w = 0 \tag{A.1}$$

The solutions u_L (Coulomb wavefunctions) then fulfill the following useful recurrence relations:

$$L\frac{du_L}{d\rho} = \sqrt{L^2+\eta^2}\, u_{L-1} - \left(\frac{L^2}{\rho} + \eta \right) u_L \tag{A.2}$$

$$(L+1)\frac{du_L}{d\rho} = \left(\frac{(L+1)^2}{\rho} + \eta \right) u_L - \sqrt{(L+1)^2+\eta^2}\, u_{L+1} \tag{A.3}$$

We want to rewrite Eq. (3.36),

$$j = \left(\frac{\partial}{\partial r}\tilde{u}_L^* \right) \left(\frac{\partial}{\partial q}\tilde{u}_L \right) - \tilde{u}_L^* \left(\frac{\partial}{\partial r}\frac{\partial}{\partial q}\tilde{u}_L \right), \tag{A.4}$$

in coordinates (η, ρ) such that it contains only partial derivatives of u_L with respect to η and terms in u_L or u_{L-1}. This can be achieved by combining the results of the first section with the recurrence relations (A.2) and (A.3):

In the new coordinates, equation (A.4) becomes

$$\begin{aligned} j &= \left(\frac{me^2}{\eta}\frac{\partial u_L^*}{\partial \rho}\right)\left[\frac{\eta}{me^2}\left(\rho\frac{\partial u_L}{\partial \rho} - \eta\frac{\partial u_L}{\partial \eta}\right)\right] \\ &\quad -u_L^*\frac{me^2}{\eta}\frac{\partial}{\partial \rho}\left[\frac{\eta}{me^2}\left(\rho\frac{\partial u_L}{\partial \rho} - \eta\frac{\partial u_L}{\partial \eta}\right)\right] \end{aligned}$$

For more convenient handling, we will treat the two terms in this expression separately:

$$j = \underbrace{\frac{\partial u_L^*}{\partial \rho}\left(\rho\frac{\partial u_L}{\partial \rho} - \eta\frac{\partial u_L}{\partial \eta}\right)}_{A} - \underbrace{u_L^*\left(\frac{\partial u_L}{\partial \rho} + \rho\frac{\partial^2 u_L}{\partial \rho^2} - \eta\frac{\partial^2 u_L}{\partial \rho \partial \eta}\right)}_{B} \tag{A.5}$$

A.2.1 Case 1: $L \neq 0$

Term A:

$$\begin{aligned} A &= \frac{\partial u_L^*}{\partial \rho}\left(\rho\frac{\partial u_L}{\partial \rho} - \eta\frac{\partial u_L}{\partial \eta}\right) \\ &= \frac{1}{L}\left(\sqrt{L^2+\eta^2}\,u_{L-1}^* - \left(\frac{L^2}{\rho}+\eta\right)u_L^*\right)\left[\frac{\rho}{L}\left(\sqrt{L^2+\eta^2}\,u_{L-1}\right.\right. \\ &\quad \left.\left. - \left(\frac{L^2}{\rho}+\eta\right)u_L\right) - \eta\frac{\partial u_L}{\partial \eta}\right] \\ &= \frac{\rho}{L^2}\left[\left(L^2+\eta^2\right)u_{L-1}^* u_{L-1} - \sqrt{L^2+\eta^2}\left(\frac{L^2}{\rho}+\eta\right)\left(u_L^* u_{L-1} + u_{L-1}^* u_L\right)\right. \\ &\quad \left. + \left(\frac{L^2}{\rho}+\eta\right)^2 u_L^* u_L\right] - \frac{\eta}{L}\left(\sqrt{L^2+\eta^2}\,u_{L-1}^*\frac{\partial u_L}{\partial \eta} - \left(\frac{L^2}{\rho}+\eta\right)u_L^*\frac{\partial u_L}{\partial \eta}\right) \end{aligned}$$

Term B:

$$B = u_L^*\left(\frac{\partial u_L}{\partial \rho} + \rho\frac{\partial^2 u_L}{\partial \rho^2} - \eta\frac{\partial^2 u_L}{\partial \rho \partial \eta}\right) = u_L^*\left(\frac{\partial u_L}{\partial \rho} + \rho\frac{\partial^2 u_L}{\partial \rho^2} - \eta\frac{\partial^2 u_L}{\partial \eta \partial \rho}\right)$$

$$
\begin{aligned}
&= u_L^* \left[\left(1 + \rho\frac{\partial}{\partial\rho} - \eta\frac{\partial}{\partial\eta}\right) \frac{1}{L} \left(\sqrt{L^2+\eta^2}\, u_{L-1} - \left(\frac{L^2}{\rho} + \eta\right) u_L \right) \right] \\
&= u_L^* \left[\frac{1}{L} \left(\sqrt{L^2+\eta^2}\, u_{L-1} - \left(\frac{L^2}{\rho} + \eta\right) u_L \right) \right. \\
&\quad + \frac{\rho}{L} \left(\sqrt{L^2+\eta^2} \frac{\partial u_{L-1}}{\partial\rho} - \left(\frac{L^2}{\rho} + \eta\right) \frac{\partial u_L}{\partial\rho} + \frac{L^2}{\rho^2} u_L \right) \\
&\quad \left. - \frac{\eta}{L} \left(\sqrt{L^2+\eta^2}\, \frac{\partial u_{L-1}}{\partial\eta} + \frac{\eta}{\sqrt{L^2+\eta^2}}\, u_{L-1} - \left(\frac{L^2}{\rho} + \eta\right) \frac{\partial u_L}{\partial\eta} - u_L \right) \right]
\end{aligned}
$$

This time we use recurrence relation (A.3) to express $\dfrac{\partial u_{L-1}}{\partial\rho}$:

$$
\begin{aligned}
B &= u_L^* \left\{ \frac{1}{L} \left(\sqrt{L^2+\eta^2}\, u_{L-1} - \left(\frac{L^2}{\rho} + \eta\right) u_L \right) \right. \\
&\quad + \frac{\rho}{L} \left[\sqrt{L^2+\eta^2} \frac{1}{L} \left(\left(\frac{L^2}{\rho} + \eta\right) u_{L-1} - \sqrt{L^2+\eta^2} u_L \right) \right. \\
&\quad \left. - \left(\frac{L^2}{\rho} + \eta\right) \frac{1}{L} \left(\sqrt{L^2+\eta^2}\, u_{L-1} - \left(\frac{L^2}{\rho} + \eta\right) u_L \right) + \frac{L^2}{\rho^2} u_L \right] \\
&\quad \left. - \frac{\eta}{L} \left(\sqrt{L^2+\eta^2} \frac{\partial u_{L-1}}{\partial\eta} + \frac{\eta}{\sqrt{L^2+\eta^2}} u_{L-1} - \left(\frac{L^2}{\rho} + \eta\right) \frac{\partial u_L}{\partial\eta} - u_L \right) \right\} \\
&= \frac{1}{L} \left(\sqrt{L^2+\eta^2}\, u_L^* u_{L-1} - \left(\frac{L^2}{\rho} + \eta\right) u_L^* u_L \right) + \\
&\quad \frac{\rho}{L^2} \left[\left(\frac{L^2}{\rho} + \eta\right)^2 u_L^* u_L + \frac{L^3}{\rho^2} u_L^* u_L - \left(L^2+\eta^2\right) u_L^* u_L \right] \\
&\quad - \frac{\eta}{L} \left(\sqrt{L^2+\eta^2}\, u_L^* \frac{\partial u_{L-1}}{\partial\eta} + \frac{\eta}{\sqrt{L^2+\eta^2}} u_L^* u_{L-1} - \left(\frac{L^2}{\rho} + \eta\right) u_L^* \frac{\partial u_L}{\partial\eta} - u_L^* u_L \right)
\end{aligned}
$$

Terms A and B have similar structure which makes it easier to see that some terms are identical and cancel in the subtraction. The final expression for $j = A - B$ for $L \neq 0$ is

$$
\begin{aligned}
j &= \frac{1}{L} \left(\left(\frac{L^2}{\rho} + \eta\right) u_L^* u_L - \sqrt{L^2+\eta^2}\, u_L^* u_{L-1} \right) \\
&\quad + \frac{\rho}{L^2} \left[\left(L^2+\eta^2\right) \left(u_{L-1}^* u_{L-1} + u_L^* u_L \right) \right.
\end{aligned}
$$

$$
\begin{aligned}
&-\sqrt{L^2+\eta^2}\left(\frac{L^2}{\rho}+\eta\right)\left(u_L^* u_{L-1}+u_{L-1}^* u_L\right)\Big] \\
&-\frac{\eta}{L}\left(\sqrt{L^2+\eta^2}\left(u_{L-1}^*\frac{\partial u_L}{\partial\eta}-u_L^*\frac{\partial u_{L-1}}{\partial\eta}\right)-\frac{\eta}{\sqrt{L^2+\eta^2}}u_L^* u_{L-1}+u_L^* u_L\right) \\
&-\frac{L}{\rho}u_L^* u_L
\end{aligned}
\tag{A.6}
$$

A.2.2 Case 2: $L = 0$

In the case $L = 0$, the steps are similar, but the other set of recursion relations has to be used. One then obtains

$$
\begin{aligned}
j \;=\; &\left(\sqrt{1+\eta^2}u_0^* u_1-\left(\frac{1}{\rho}+\eta\right)u_0^* u_0\right) \\
&+\rho\left[(1+\eta^2)(u_1^* u_1+u_0^* u_0)-\sqrt{1+\eta^2}\left(\frac{1}{\rho}+\eta\right)\left(u_1^* u_0+u_0^* u_1\right)\right] \\
&-\eta\left[\frac{\eta}{\sqrt{1+\eta^2}}u_0^* u_1-\sqrt{1+\eta^2}\left(u_1^*\frac{\partial u_0}{\partial\eta}-u_0^*\frac{\partial u_1}{\partial\eta}\right)-u_0^* u_0\right] \\
&+\frac{1}{\rho}u_0^* u_0
\end{aligned}
\tag{A.7}
$$

Appendix B

Particles used in the Thermal Model

particle	I_3	baryon number	strangeness	A	mass [MeV]
π^0	0	0	0	1	135
π^+	1	0	0	1	139.6
π^-	-1	0	0	1	139.6
η	0	0	0	2	547.5
ρ^0	0	0	0	2	769.9
ρ^+	1	0	0	2	769.9
ρ^-	-1	0	0	2	769.9
ω	0	0	0	2	781.9
η'	0	0	0	2	957.8
ϕ	0	0	0	2	1019.4

particle	I_3	baryon number	strangeness	A	mass [MeV]
K^0	-1/2	0	1	1	497.7
$K^{\sim 0}$	1/2	0	-1	1	497.7
K^+	1/2	0	1	1	493.7
K^-	-1/2	0	-1	1	493.7
K^{*0}	-1/2	0	1	2	896.1
$K^{*\sim 0}$	1/2	0	-1	2	896.1
K^{*+}	1/2	0	1	2	891.6
K^{*-}	-1/2	0	-1	2	891.6
Λ^0	0	1	-1	1	1115.7
$\Lambda^{\sim 0}$	0	-1	1	1	1115.7
n	-1/2	1	0	1	939.6
$n^{\sim}$	1/2	-1	0	1	939.6
p	1/2	1	0	1	938.3
$p^{\sim}$	-1/2	-1	0	1	938.3
Σ^+	1	1	-1	1	1189.4
$\Sigma^{\sim -}$	-1	-1	1	1	1189.4
Σ^0	0	1	-1	1	1192.6
$\Sigma^{\sim 0}$	0	-1	1	1	1192.6
Σ^-	-1	1	-1	1	1197.4
$\Sigma^{\sim +}$	1	-1	1	1	1197.4

particle	I_3	baryon number	strangeness	A	mass [MeV]
Ξ^0	1/2	1	-2	1	1314.9
$\Xi^{\sim 0}$	-1/2	-1	2	1	1314.9
Ξ^-	-1/2	1	-2	1	1321.3
$\Xi^{\sim +}$	1/2	-1	2	1	1321.3
Δ^{++}	3/2	1	0	2	1232
$\Delta^{\sim --}$	-3/2	-1	0	2	1232
Δ^+	1/2	1	0	2	1232
$\Delta^{\sim -}$	-1/2	-1	0	2	1232
Δ^0	-1/2	1	0	2	1232
$\Delta^{\sim 0}$	1/2	-1	0	2	1232
Δ^-	-3/2	1	0	2	1232
$\Delta^{\sim +}$	3/2	-1	0	2	1232
Σ^{*+}	1	1	-1	2	1383
$\Sigma^{*\sim -}$	-1	-1	1	2	1383
Σ^{*0}	0	1	-1	2	1384
$\Sigma^{*\sim 0}$	0	-1	1	2	1384
Σ^{*-}	-1	1	-1	2	1387
$\Sigma^{*\sim +}$	1	-1	1	2	1387
Ξ^{*0}	1/2	1	-2	2	1530
$\Xi^{*\sim 0}$	-1/2	-1	2	2	1530

particle	I_3	baryon number	strangeness	A	mass [MeV]
Ξ^{*-}	-1/2	1	-2	2	1530
$\Xi^{*\sim+}$	1/2	-1	2	2	1530
Ω^{-}	0/2	1	-3	1	1672.5
$\Omega^{\sim+}$	0/2	-1	3	1	1672.5

BIBLIOGRAPHY

Bibliography

[1] Milton Abramowitz and Irene A. Stegun. *Handbook of Mathematical Functions*. National Bureau of Standards, seventh printing, 1st edition, 1968.

[2] D. Adamova et al. Enhanced production of low-mass electron pairs in 40-a-gev pb au collisions at the cern sps. 2002, nucl-ex/0209024.

[3] J. Adams et al. Evidence from d + au measurements for final-state suppression of high p(t) hadrons in au + au collisions at rhic. 2003, nucl-ex/0306024.

[4] J. Adams et al. Narrowing of the balance function with centrality in au + au collisions s(nn)**(1/2) = 130-gev. *Phys. Rev. Lett.*, 90:172301, 2003, nucl-ex/0301014.

[5] J. Adams et al. Transverse momentum and collision energy dependence of high p(t) hadron suppression in au + au collisions at ultrarelativistic energies. 2003, nucl-ex/0305015.

[6] C. Adler et al. Pion interferometry of s(nn)**(1/2) = 130-gev au + au collisions at rhic. *Phys. Rev. Lett.*, 87:082301, 2001, nucl-ex/0107008.

[7] C. Adler et al. Disappearance of back-to-back high p(t) hadron correlations in central au + au collisions at s(nn)**(1/2) = 200-gev. *Phys. Rev. Lett.*, 90:082302, 2003, nucl-ex/0210033.

[8] G. Agakishiev et al. Low-mass e+ e- pair production in 158-a-gev pb au collisions at the cern sps, its dependence on multiplicity and transverse momentum. *Phys. Lett.*, B422:405–412, 1998, nucl-ex/9712008.

[9] D. Anchishkin, Ulrich W. Heinz, and P. Renk. Final state interactions in two-particle interferometry. *Phys. Rev.*, C57:1428–1439, 1998, nucl-th/9710051.

[10] R. Baier, Yuri L. Dokshitzer, Alfred H. Mueller, and D. Schiff. Radiative energy loss of high energy partons traversing an expanding QCD plasma. *Phys. Rev.*, C58:1706–1713, 1998, hep-ph/9803473.

[11] R. Baier, Yuri L. Dokshitzer, Alfred H. Mueller, and D. Schiff. On the angular dependence of the radiative gluon spectrum. *Phys. Rev.*, C64:057902, 2001, hep-ph/0105062.

[12] R. Baier, Yuri L. Dokshitzer, S. Peigne, and D. Schiff. Induced gluon radiation in a qcd medium. *Phys. Lett.*, B345:277–286, 1995, hep-ph/9411409.

[13] Steffen A. Bass, Pawel Danielewicz, and Scott Pratt. Clocking hadronization in relativistic heavy ion collisions with balance functions. *Phys. Rev. Lett.*, 85:2689–2692, 2000, nucl-th/0005044.

[14] Gordon Baym and Peter Braun-Munzinger. Physics of coulomb corrections in hanbury-brown-twiss interferometry in ultrarelativistic heavy ion collisions. *Nucl. Phys.*, A610:286c–296c, 1996, nucl-th/9606055.

[15] Jean-Paul Blaizot. Signals of the quark-gluon plasma in nucleus nucleus collisions. *Nucl. Phys.*, A661:3–12, 1999, hep-ph/9909434.

[16] P. Braun-Munzinger, D. Magestro, K. Redlich, and J. Stachel. Hadron production in au au collisions at rhic. *Phys. Lett.*, B518:41–46, 2001, hep-ph/0105229.

[17] A. Capella, J. A. Casado, C. Pajares, A. V. Ramallo, and J. Tran Thanh Van. Nuclear effects in j / psi suppression. *Phys. Lett.*, B206:354, 1988.

[18] Nucleon-kaon and nucleon-pion phase shifts are available on-line from the Center for Nuclear Studies, Data Analysis Center at George Washington University. http://gwdac.phys.gwu.edu/.

[19] K.C. Chase and A.Z. Mekjian. Exact methods for expectation values in canonical fragmentation models. *Phys. Rev. C*, 52:2339, 1995.

[20] Sen Cheng and Scott Pratt. Isospin fluctuations from a thermally equilibrated hadron gas. *Phys. Rev.*, C67:044904, 2003, nucl-th/0207051.

[21] P. Danielewicz et al. Disappearance of elliptic flow: A new probe for the nuclear equation of state. *Phys. Rev. Lett.*, 81:2438–2441, 1998, nucl-th/9803047.

[22] Pawel Danielewicz. Nuclear equation of state. 2001, nucl-th/0112006.

[23] S. Das Gupta and A.Z. Mekjian. Phase transition in a statistical model for nuclear multifragmentation. *Phys. Rev. C*, 57:1361, 1998.

[24] Herbert Goldstein. *Classical Mechanics*, page 102. Addison Wesley, 3rd ed edition, 2002.

[25] M. Gyulassy, I. Vitev, and X. N. Wang. High p(t) azimuthal asymmetry in noncentral a + a at rhic. *Phys. Rev. Lett.*, 86:2537–2540, 2001, nucl-th/0012092.

[26] Miklos Gyulassy and Sandra S. Padula. Kaon versus pion interferometry signatures of quark - gluon plasma formation. *Phys. Rev.*, C41:21, 1990.

[27] Miklos Gyulassy and Xin-nian Wang. Multiple collisions and induced gluon bremsstrahlung in qcd. *Nucl. Phys.*, B420:583–614, 1994, nucl-th/9306003.

[28] R. Hanbury Brown and R. Q. Twiss. A new type of interferometer for use in radio astronomy. *Phil. Mag.*, 45:663–682, 1954.

[29] Ulrich W. Heinz and Barbara V. Jacak. Two-particle correlations in relativistic heavy-ion collisions. *Ann. Rev. Nucl. Part. Sci.*, 49:529–579, 1999, nucl-th/9902020.

[30] Klaus Jänich. *Analysis für Physiker und Ingenieure*, page 286. Springer, 3rd edition, 1995.

[31] B.K. Jennings, D.H. Boal, and J.C. Shillcock. Two-particle correlation functions in the thermal model and nuclear interferometry descriptions. *Phys. Rev. C*, 33:1303, 1986.

[32] Sang-yong Jeon and Scott Pratt. Balance functions, correlations, charge fluctuations and interferometry. *Phys. Rev.*, C65:044902, 2002, hep-ph/0110043.

[33] F. Karsch and E. Laermann. Thermodynamics and in-medium hadron properties from lattice qcd. 2003, hep-lat/0305025.

[34] F. Karsch, E. Laermann, and A. Peikert. The pressure in 2, 2+1 and 3 flavour qcd. *Phys. Lett.*, B478:447–455, 2000, hep-lat/0002003.

[35] Y. D. Kim, R. T. de Souza, et al. Final-state coulomb interactions for intermediate-mass fragment emission. *Phys. Rev.*, C45:387–395, 1992.

[36] P. Koch, B. Muller, and J. Rafelski. Strangeness in relativistic heavy ion collisions. *Phys. Rept.*, 142:167–262, 1986.

[37] Peter F. Kolb and Ulrich Heinz. Hydrodynamic description of ultrarelativistic heavy-ion collisions. 2003, nucl-th/0305084.

[38] S. E. Koonin. Proton pictures of high-energy nuclear collisions. *Phys. Lett.*, B70:43–47, 1977.

[39] R. Kotte et al. On the space-time difference of proton and composite particle emission in central heavy-ion reactions at 400-a- mev. *Eur. Phys. J.*, A6:185–195, 1999, nucl-ex/9904007.

[40] L. D. Landau and E.M. Lifshitz. *Quantum Mechanics*, volume volume 3 of *Course of Theoretical Physics*. Addison Wesley, 1st english edition, 1958.

[41] R. Lednicky, V. L. Lyuboshitz, B. Erazmus, and D. Nouais. How to measure which sort of particles was emitted earlier and which later. *Phys. Lett. B*, B373:30–34, 1996.

[42] T. Matsui and H. Satz. J / psi suppression by quark - gluon plasma formation. *Phys. Lett.*, B178:416, 1986.

[43] Albert Messiah. *Quantum Mechanics*, volume volume I. North-Holland Publishing Company, 1st english edition, 1958.

[44] S. Pratt. Pion interferometry of quark - gluon plasma. *Phys. Rev.*, D33:1314–1327, 1986.

[45] S. Pratt. Two particle and multiparticle measurements for the quark - gluon plasma. In R. C. Hwa, editor, *Quark-Gluon Plasma 2*, pages 700–748. World Scientific, 1995.

[46] S. Pratt. Balance functions: A signal of late-stage hadronization. *Nucl. Phys.*, A698:531–534, 2002.

[47] S. Pratt. Correlations and fluctuations, a summary of quark matter 2002. *Nucl. Phys.*, A715:389–398, 2003.

[48] S. Pratt, T. Csoergoe, and J. Zimanyi. Detailed predictions for two pion correlations in ultrarelativistic heavy ion collisions. *Phys. Rev.*, C42:2646–2652, 1990.

[49] Scott Pratt and Sen Cheng. Removing distortions from charge balance functions. *Phys. Rev.*, C68:014907, 2003, nucl-th/0303025.

[50] Scott Pratt, Sen Cheng, et al. Modeling charge balance functions. *to be published.*

[51] Scott Pratt and Silvio Petriconi. Alternative size and lifetime measurements for high-energy heavy-ion collisions. 2003, nucl-th/0305018.

[52] Scott Pratt and Jorg Ruppert. The quark-gluon plasma in a finite volume. *to appear in Phys. Rev. C*, 2003, nucl-th/0303043.

[53] Johann Rafelski and Jean Letessier. Strangeness and quark gluon plasma. 2003, hep-ph/0305284.

[54] Dirk H. Rischke and Miklos Gyulassy. The time-delay signature of quark-gluon plasma formation in relativistic nuclear collisions. *Nucl. Phys.*, A608:479–512, 1996, nucl-th/9606039.

[55] P. J. Siemens and S. A. Chin. Testing of qcd plasma formation by dilepton spectra in relativistic nuclear collisions. *Phys. Rev. Lett.*, 55:1266–1268, 1985.

[56] Sven Soff, Steffen A. Bass, and Adrian Dumitru. Pion interferometry at rhic: Probing a thermalized quark gluon plasma? *Phys. Rev. Lett.*, 86:3981–3984, 2001, nucl-th/0012085.

[57] H. Sorge. Highly sensitive centrality dependence of elliptic flow: A novel signature of the phase transition in qcd. *Phys. Rev. Lett.*, 82:2048–2051, 1999, nucl-th/9812057.

[58] S. Voloshin, R. Lednicky, S. Panitkin, and Nu Xu. Relative space-time asymmetries in pion and nucleon production in noncentral nucleus nucleus collisions at high energies. *Phys. Rev. Lett.*, 79:4766–4769, 1997, nucl-th/9708044.

[59] Johannes P. Wessels et al. Latest results from ceres/na45. *Nucl. Phys.*, A715:262–271, 2003, nucl-ex/0212015.

[60] Urs Achim Wiedemann, Daniel Ferenc, and Ulrich W. Heinz. Coulomb final state interactions for gaussian wave packets. *Phys. Lett.*, B449:347–353, 1999, nucl-th/9811103.

[61] Urs Achim Wiedemann and Ulrich W. Heinz. Particle interferometry for relativistic heavy-ion collisions. *Phys. Rept.*, 319:145–230, 1999, nucl-th/9901094.